

Modeling a Realistic Dynamical Model for High Energy Heavy Ion Collisions

Chiho NONAKA^{1,2*)} and Masayuki ASAKAWA^{3**)}

¹*Kobayashi-Maskawa Institute for the Origin of Particles and the Universe (KMI),*

²*Department of Physics, Nagoya University,*

Furo-cho, Chikusa-ku, Nagoya 464-8602, Japan

³*Physics Department, Osaka University, Toyonaka 560-0043, Japan*

In this article, we outline the modeling of a realistic dynamical model for comprehensive description of high energy heavy ion collisions. Comparing theoretical calculations and experimental data at RHIC, we give detailed discussions on the key ingredients for the construction of a multi-module model: initial condition, hydrodynamical expansion, hadronization, and freezeout processes.

§1. Introduction

Since the Relativistic Heavy Ion Collider (RHIC) at Brookhaven National Laboratory (BNL) started its operation in 2000, a lot of discovery has been made and a lot of insight related to quantum chromodynamics (QCD) phase transition and the Quark-Gluon Plasma (QGP) has been gained. One of the most physically interesting and surprising outcomes at RHIC is the production of the strongly interacting QGP (sQGP). This accomplishment was realized by combining investigations from both experimental¹⁾ and theoretical²⁾ sides. Because the QGP had been believed to be a weakly interacting system like the ideal gas, the discovery of sQGP opened up a new paradigm for the understanding of high temperature and/or high density QCD.

The highlights of the RHIC experiments were (i) strong elliptic flow, which suggests early thermalization and early formation of collectivity; (ii) strong jet quenching, which confirms the formation of hot and dense matter in collisions; (iii) constituent quark number scaling of the elliptic flow, which indicates the formation of deconfined hot quark soup.¹⁾ From studies of these experimental results with relativistic hydrodynamical models, jet energy loss mechanism, and recombination models, the discovery of sQGP at RHIC²⁾ was accomplished. Furthermore, heavy ion collision operation at the Large Hadron Collider (LHC), whose collision energy is around 15 times as large as that at RHIC, started in 2010. Such a high energy collision experiment gives us an opportunity to perform further investigation on the QCD diagram.

Figure 1 shows a schematic sketch of the time evolution in relativistic heavy ion collisions on the basis of present understanding. When two heavy ions are accelerated to high energy, an extreme state which is described by static color charge and classical gluon fields, called the color glass condensate (CGC) state, is realized

*) nonaka@hken.phys.nagoya-u.ac.jp

**) yuki@phys.sci.osaka-u.ac.jp

inside each heavy ion. At the collision of the two heavy ions, high energy prompt photons and Drell-Yan dileptons, and jets are produced by hard scattering of quarks and gluons. After the collision thermalization is achieved in a short time. During that time, prethermal photons and dileptons are created and the entropy of the fireball increases. If the collision energy is large enough, QGP is also produced at this stage. Then hydrodynamical expansion starts, and a lot of interesting physical processes occur: collective flow formation, jet quenching, production of thermal photons and dileptons, and so on. As the temperature and density of the fireball decreases, hadronization of the QGP phase takes place. To understand the hadronization mechanism in relativistic heavy ion collisions, the recombination/coalescence mechanism and the fragmentation mechanism are employed. Gradually the mean free path between hadrons becomes large, and eventually freezeout happens. At this stage, final state interactions play an important role.

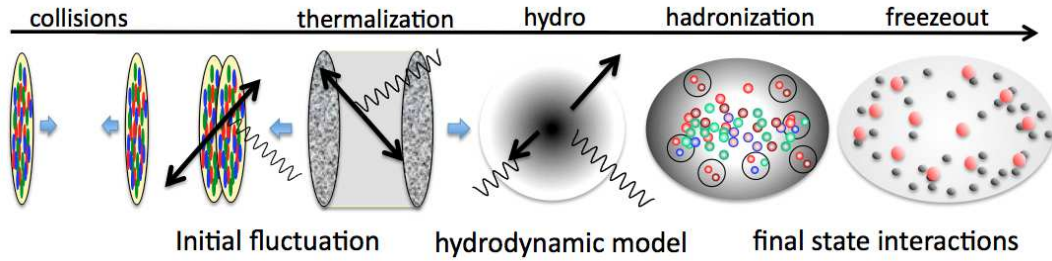


Fig. 1. Schematic sketch of relativistic heavy ion collisions. The wavy lines stand for photons and the arrows stand for jets.

The present understanding of heavy ion collisions strongly suggests (Fig. 1) that a multi-module modeling is indispensable for the description of entire history of heavy ion collisions. Knowledge of dominant physics at each stage has been accumulated, but a comprehensive model is still missing. For the construction of such a multi-module model, hydrodynamical models are a promising starting point, because at present it is considered as one of the most reliable and successful dynamical models for understanding experimental data at RHIC and LHC comprehensively, especially for the description of the QGP phase. At the same time, it is easy to implement the latest developments in the physics of heavy ion collisions such as fluctuated initial conditions, the lattice QCD inspired equation of state, recombination mechanism for hadronization, and final state interactions in freezeout processes into a hydrodynamical model, as we will describe later in detail.

In Tabs. I and II current hydrodynamical models are listed. In line with the physical picture shown in Fig. 1, in particular, we pick up and compare the following features of each hydrodynamical model: dimension of hydrodynamical expansion (dim), initial condition (IC), equation of state (EoS), and treatment of freezeout process. In addition, we also compare the numerical schemes in solving the relativistic hydrodynamical equation and observables calculated in each model in the tables. The importance of utilizing proper numerical schemes in solving the relativistic hydrodynamical equation will be discussed in Sec. 4. Recent development

in relativistic viscous hydrodynamical models is remarkable. From the point of view of multi-module modeling, however, the status of ideal hydrodynamical models is considered to be more mature.

Table I. Ideal hydrodynamical models. In the table, we use the following abbreviation. IC: initial condition, G: Glauber model, CGC: color glass condensate, MC-G: Monte Carlo Glauber model, MC-CGC: Monte Carlo CGC, IQCD: lattice QCD inspired EoS, SPH: smoothed particle hydrodynamics, PPM: piecewise parabolic method, CE: continuous emission, Obs: calculated observables, and PD: particle distribution.

Ref.	dim	IC	EoS	scheme	freezeout	Obs
Hama ³⁾	3+1	NeXus	Bag model	SPH	CE	PD, v_2 , HBT
Hirano ⁴⁾	3+1	G, CGC	Bag model	PPM ^{**)}	cascade(JAM)	v_2
Nonaka ⁸⁾	3+1	G	Bag model	Lagrange	cascade(UrQMD)	PD, v_2
Hirano ^{9), 10)}	3+1	MC-G, MC-CGC	lQCD	PPM ^{**)}	cascade(JAM)	v_2
Petersen ¹¹⁾	3+1	UrQMD	hadron gas	SHASTA	cascade(UrQMD)	PD
Holopainen ¹²⁾	2+1	MC-G	lQCD	SHASTA	resonance decay	v_2

Table II. Viscous hydrodynamical models. In the table, we use the following abbreviation. CD: central difference, and KT: Kurganov-Tadmor (KT) scheme.

Ref.	dim	IC	EoS	scheme	freezeout	Obs.
Romatschke ¹³⁾	2+1	G	lQCD	CD	single T_f	v_2
Dusling ¹⁴⁾	2+1	G	ideal gas	—	viscous correction	v_2
Luzum ¹⁵⁾	2+1	G, CGC	lQCD	CD	resonance decay	v_2
Schenke ¹⁶⁾	3+1	MC-G	lQCD	KT	viscous correction	v_2, v_3
Song ¹⁷⁾	2+1	MC-G, MC-CGC	lQCD	SHASTA	cascade(UrQMD)	v_2
Chaudhuri ^{18), 19)}	2+1	G	Bag model	SHASTA	viscous correction	v_2
Bozek ²⁰⁾	3+1	G	lQCD	—	THERMINATOR2	v_1, v_2 , HBT

In this article, we outline the modeling of a realistic dynamical model for the description of relativistic heavy ion collisions in line with the physical picture shown by the schematic sketch (Fig. 1). In the discussion, we refer to and compare with experimental data at SPS, RHIC, and LHC. The article is organized as follows. In Sec. 2, we review the initial condition for hydrodynamical models from the conventional Glauber type one to the latest attempt to include event-by-event fluctuated initial conditions. In Sec. 3, we present the basic concepts and ingredients of both ideal and viscous hydrodynamics such as relativistic hydrodynamical equation, equations of state, and transport coefficients. We will also discuss interplay among jets, medium, and hydrodynamical expansion. In Sec. 4, we review the numerical schemes which are listed in Tabs. I and II and show the result of the newly developed scheme by one of the authors and her collaborators for a relativistic viscous hydrodynamical

^{**)} It is now customary in numerical hydrodynamics not to call a hydrodynamical computer program a PPM (piecewise parabolic method)⁵⁾ one unless it fulfills not only parabolic interpolation of variables but also sharpening of discontinuity profiles and flattening of post-shock oscillations.⁶⁾ Hirano's code^{4), 9), 10)} executes only the first of the above three ingredients.⁷⁾ Attention needs to be paid on this difference when comparing with other PPM codes and estimating its capability to capture shocks.

model. In Sec. 5, we explain the recombination model and show its utility in understanding hadron observables and the QCD phase diagram. In Sec. 6, we explain chemical and thermal freezeout processes and discuss effects of final state interactions by comparing theoretical calculation and experimental data. Section 7 is devoted to summary and conclusions.

§2. Initial conditions

The hydrodynamical equations of motion requires inputs of initial conditions for all their dynamical variables, which are then evolved forward in time. These initial conditions are outside of the framework of hydrodynamical models and have to be determined by other means. Physically, they are determined by the process during the initial collision of the nuclei and the succeeding stage that makes the system approach to equilibrium, which is eventually reached at a time τ_0 . Note that τ_0 , in principle, can depend on the coordinate space rapidity η , while in practice it is assumed to be independent of η . The equilibration time is a parameter since the equilibration mechanisms are still under debate and the first principle determination of the initial conditions of the equilibrated plasma phase has not been achieved.^{(21), (22)}

Historically, parameterized initial conditions for entropy density (or alternatively the energy densities) and the net baryon density have been used.^{(8), (23), (24), (25)} In the transverse plane these distributions have been mainly parameterized based on Glauber-type models of nuclear collisions. In the longitudinal direction initial distributions inspired by Bjorken's scaling solution are often used. Then a few parameters remain to be fixed additionally in the initial condition, such as the maximum values of the energy or entropy density, and net baryon density. They are usually fixed by comparison with experimental data on single particle rapidity distributions and transverse momentum spectra.

As a first trial, one can choose to set the initial longitudinal flow to Bjorken's scaling solution,⁽²⁶⁾ and one can set the initial transverse flow to zero. This simplest initial flow profile has served as the basis for all further investigation. The possibility of the existence of an initial transverse flow at τ_0 was discussed, e.g., by Kolb and Rapp.⁽²⁷⁾ The initial flow improves the results for P_T -spectra and reduces the anisotropy. This suggests that HBT analyses may be a sensitive tool for the determination of the initial longitudinal flow. We note that, for the analysis of the final state longitudinal flow, the Yano-Koonin parametrization is effective. Hydrodynamical calculations during the early RHIC years did show serious disagreement with experimental data, especially for the ratio of $R_{\text{out}}/R_{\text{side}}$, leading to the notion of the HBT puzzle.⁽²⁸⁾ It turned out that the solution of the HBT puzzle is not so simple because it is related to all stages of hydrodynamical model: initial conditions, the equation of state, viscosity effect, and final state interactions. Pratt⁽²⁹⁾ showed that this HBT puzzle comes from not a single shortcoming of hydrodynamical models, but the combination of several effects; it is solved by mainly prethermal acceleration, a stiffer equation of state, and viscosity effect.

Let us come back to the apparent early thermalization times found at RHIC. Usually it is argued that small initial times τ_0 are needed to describe the elliptic

flow data as the elliptic flow builds up at the earliest stage of expansion when the eccentricity of the fireball is largest.^{30),31)} However, we note that with suitable sets of initial conditions and freezeout temperatures in fact a larger initial proper time is also compatible with data. Luzum and Romatschke show that three very different sets of the initial and freezeout temperature (T_i, T_f) — (0.29, 0.14) GeV with $\tau_0 = 2$ fm, (0.36, 0.15) GeV with $\tau_0 = 1$ fm, and (0.43, 0.16) GeV with $\tau_0 = 0.5$ fm — provide almost identical differential elliptic flows in their viscous hydrodynamical calculation.¹⁵⁾ This suggests that better constraints on initial conditions are indispensable to avoid incorrect conclusions from comparisons of hydrodynamical calculations with experimental data.

Other approaches have been also taken in generating initial conditions. Color glass condensate-inspired initial conditions are becoming increasingly popular (Tabs. I and II). They feature larger eccentricities of the initial energy profile than Glauber-based models, which has significant implications on elliptic flow.³²⁾ In these models additional dissipation during the early quark-gluon plasma stage is needed in order to achieve agreement with experiments.^{32),4)} Others models include the string rope model³³⁾ and the pQCD + saturation model.³⁴⁾ In the latter the initial time τ_0 is given by the inverse of the saturation scale, which is very small, i.e., $\tau = 0.18$ (0.10) fm at RHIC (LHC).

More recently there is a push to implement effects of event-by-event fluctuations in the initial conditions. In the NEXSPHERIO hydro model each event is created by the event generator NeXus.³⁾ First they found that the existence of fluctuation in initial conditions improves the behavior of the elliptic flow as a function of the rapidity in hydrodynamical calculation.³⁵⁾ They showed that the two artificial bumps in the elliptic flow as a function of the rapidity²⁴⁾ disappear if they take into account of initial fluctuations.

An interesting observable, “Mach-Cone-like structure”, which is an angular correlation with the leading jet particle was reported at RHIC.^{36),37)} At first the origin of the structure is considered as the remnant of the interactions between jets and medium ([18]–[26] in Ref.³⁶⁾). Models succeeded in giving the qualitative interpretation of the structure, but they are not so successful in quantitatively describing the experimental data. For the first time in Ref.³⁸⁾ event-by-event fluctuations in the initial state were considered as a possible origin of the structure. A breakthrough of clear understanding of the Mach-Cone-like structure was done by detailed experimental analyses of triangular flow and higher harmonics. Current understanding is that the Mach-Cone-like structure is dominated by the triangular flow (See for example, Ref.³⁹⁾). The triangular flow and higher harmonics are the coefficients in the Fourier expansion of particle yields as a function of the azimuthal angle ϕ ,

$$\frac{dN}{dyd\phi} \propto 1 + 2v_1 \cos(\phi - \Theta_1) + 2v_2 \cos 2(\phi - \Theta_2) + 2v_3 \cos 3(\phi - \Theta_3) + 2v_4 \cos 4(\phi - \Theta_4) + \dots, \quad (2.1)$$

where v_1 , v_2 , v_3 , and v_4 are directed, elliptic, triangular, and quadrangular flows, respectively. $\Theta_i (i = 1, 2, \dots)$ are constants and in principle independent from each other. The origin of the triangular flow and higher harmonics is fluctuation in initial

conditions⁴⁰⁾ (Fig. 2). In particular, v_3 vanishes, if the system starts with a smooth almond-shaped initial state⁴⁰⁾ (Fig. 3). Investigation of the relation between initial geometry and higher harmonics has been also carried out.⁴¹⁾ For more quantitative analyses, however, contributions of final state interactions should be evaluated.

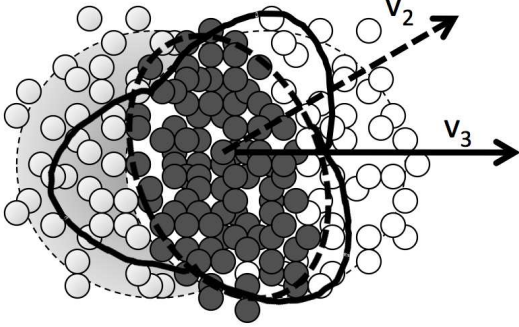


Fig. 2. Elliptic and triangular flows from fluctuated initial state.

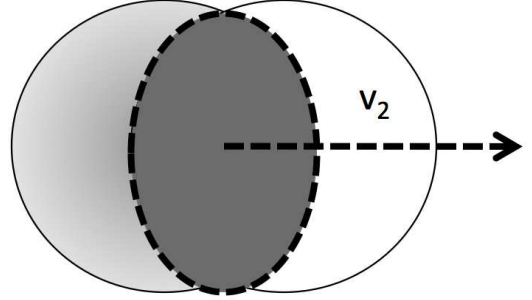


Fig. 3. Elliptic flow from a smooth almond-shaped initial state.

Here we make a comment on event-by-event fluctuations in the initial conditions in hydrodynamical models from the point of view of the numerical solution of the hydrodynamical equation. When the hydrodynamical simulation is performed with initial conditions with the event-by-event fluctuation, shock-wave capturing schemes should be used to describe the hydrodynamical expansion correctly. Otherwise, the effect of the fluctuation is smeared. It is known that most of the numerical schemes used in the calculations of the time evolution of the quark-gluon plasma do not satisfy this requirement. In other words, they introduce numerical viscosity to a non-negligible extent. In the early stage of the RHIC operation, hydrodynamical models gave us certain evidence of the existence of strongly interacting QGP at RHIC and are eventually regarded as the most reliable dynamical models for high energy heavy ion collisions. However, recent high statistical experimental data impose more rigorous numerical treatment on the hydrodynamical models. We will discuss this issue in detail later in Sec. 4.

2.1. Experimental Data and Discussion

Among various kinds of experimental observables, thermal photons are one of the most promising ones for the investigation of the initial conditions of hydrodynamic models. PHENIX Collaboration reported that the excess from the superposition of pp collisions in its direct photon measurement at low transverse momentum P_T . This excess follows the exponential distribution, which suggests that the thermal equilibrium is achieved.⁴²⁾ They extract the inverse-slope parameter from the photon spectra in Au+Au $\sqrt{s} = 200$ GeV, $T = 221 \pm 19^{\text{stat}} \pm 19^{\text{syst}}$. This value is larger than the critical temperature of the phase transition (~ 160 MeV), but it is smaller than the initial temperatures of hydrodynamic models at RHIC, $T \sim 300 - 600$ MeV. The value is interpreted as the average temperature in the whole hydrodynamic expansion. Contributions from the hadron phase are also important.

It will be appropriate to point out here the importance of the hydro+micro

model as an instrument that relates the initial state condition to the final state observables. Very often, for example, final state multiplicities are directly predicted from the initial condition from the color glass condensate picture. For example, when the first LHC multiplicity data came out,⁴³⁾ deviation of the experimental data from the prediction of the color glass condensate picture was found and was regarded as a serious problem. In fact, the system goes through several processes in which entropy and multiplicity change, such as the thermalization of the quark-gluon plasma, entropy production in the quark-gluon plasma, hadronization, and resonance production in the hadron phase and their decays. It is thus to be emphasized that the understanding of the final state observables requires the understanding of the whole period of the time evolution in heavy ion collisions. We will come back to this issue in Sec. 6.

§3. Hydrodynamical expansion

In the early stage of the RHIC operation, only hydrodynamical models were able to explain the strong elliptic flow,⁴⁴⁾ which was solid evidence of the creation of the strongly interacting QGP at RHIC. However, detailed analyses on experimental data eventually revealed the limitations of hydrodynamical models. They have difficulty in explaining, for example, the elliptic flow at forward/backward rapidity, HBT results, the centrality dependence of elliptic flow, and so forth. At the same time, viscosities became one of the most central topics in relativistic heavy ion collisions, while most of analyses had been carried out with ideal hydrodynamics. After the discovery of the strongly interacting QGP, the main interest at RHIC shifted to the understanding of detailed properties of the strongly interacting QGP.

3.1. Hydrodynamical equations

The basis of hydrodynamical models is the energy and momentum conservation,

$$\partial_\mu T^{\mu\nu}(x) = 0, \quad (3.1)$$

where $T^{\mu\nu}(x)$ is the energy momentum tensor. In the case of ideal relativistic fluid, the energy momentum tensor is given by

$$T^{\mu\nu}(x) = [\epsilon(x) + p(x)]u^\mu(x)u^\nu(x) - p(x)g^{\mu\nu}, \quad (3.2)$$

where $\epsilon(x)$, $p(x)$, and $u^\mu(x)$ are the energy density, pressure, and four velocity, respectively. Eq. (3.1) is solved numerically simultaneously with the charge conservation relation,

$$\partial_\mu j^\mu(x) = 0. \quad (3.3)$$

When one starts to include the effects of dissipation into relativistic hydrodynamics, one is confronted with a rather complicated situation. One of the difficulties is that naive introduction of viscosities, first order theory (i.e., first order in gradients) suffers from acausality. The heat conduction equation allows instantaneous propagation of heat because of its parabolicity. The acausality of first order hydrodynamics stems from the same reason. In order to avoid this problem, second

order terms in heat flow and viscosities have to be included in the expression for the entropy,^{45), 46), 47), 48), 49), 50), 51)} but the systematic treatment of these second order terms has not been established. Although there is remarkable progress toward the construction of a fully consistent relativistic viscous hydrodynamical theory, there are still ongoing discussions about the formulation of the equations of motion and about the numerical procedures.⁵²⁾

The basic tenet that has to be given up in dissipative hydrodynamics is the assumption of a uniquely defined local rest frame. Away from equilibrium the vectors defining the flows of energy, momentum, and conserved charges can be misaligned. We can still define a local rest frame by just choosing a velocity $u^\mu(x)$ in the laboratory frame. Then the energy-momentum tensor and the conserved charge current take more general involved forms,

$$T^{\mu\nu}(x) = [\epsilon(x) + p(x) + \Pi(x)]u^\mu(x)u^\nu(x) - [p(x) + \Pi(x)]g^{\mu\nu} + 2W^{(\mu}u^{\nu)} + \pi^{\mu\nu}, \quad (3.4)$$

$$j^\mu(x) = n(x)u^\mu + V^\mu, \quad (3.5)$$

where V^μ and W^μ are corrections to the flow of conserved charge and energy that are orthogonal to u^μ and $T^{\mu\nu}u_\nu$, respectively, $\pi^{\mu\nu}$ (with the orthogonality conditions $u_\mu\pi^{\mu\nu} = \pi^{\mu\nu}u_\nu = 0$) is the symmetric traceless shear stress tensor, and Π is the bulk stress. (\cdots) indicates the symmetrization with regard to the indices. Usually u^μ is chosen to define one of the two standard frames: the Eckart frame where the velocity is given by the physical flow of net charge (then $V^\mu = 0$), or the Landau frame where the velocity is given by the energy flow (then $W^\mu = 0$). We refer the reader to the article by Muronga and Rischke for further discussions.⁵³⁾

At first order the new structures are proportional to gradients of the velocity field u^μ , and only three proportionality constants appear: the shear viscosity η , the bulk viscosity ζ , and the heat conductivity κ . With the usual definitions the first order relations in the Landau frame are⁵³⁾

$$\Pi = -\zeta\nabla_\mu u^\mu, \quad (3.6)$$

$$q^\mu = -\kappa\frac{nT^2}{e+p}\nabla^\mu\frac{\mu}{T}, \quad (3.7)$$

$$\pi^{\mu\nu} = 2\eta\nabla^{<\mu}u^{\nu>}, \quad (3.8)$$

where $q^\mu = -(\epsilon + p)/nV^\mu$ is the heat flow, $\nabla^\mu = (g^{\mu\nu} - u^\mu u^\nu)\partial_\nu$ is the covariant derivative orthogonalized to the flow vector, T and μ are the temperature and chemical potential for the conserved charge, respectively. Here only one conserved charge is assumed, but the extension to cases with more than two conserved charges is straightforward. $\langle\cdots\rangle$ refers to the symmetrization of indices with the trace subtracted. The entropy current S^μ receives additional contributions beyond the equilibrium term su^μ and one can show that all three transport coefficients are positive, demanding that the entropy is strictly non-decreasing, $\partial_\mu S^\mu \geq 0$.

At second order many more new parameters, related to relaxation phenomena, appear. Currently, most of viscous hydrodynamical calculations use the relativistic dissipative equations of motion that were derived phenomenologically by Israel

and Stewart⁴⁸⁾ and variants of those, while some use the method by Öttinger and Grmela.^{49), 50), 51)} See for example Ref.¹⁴⁾ Recently, a second-order viscous hydrodynamics from AdS/CFT correspondence was derived,⁵⁴⁾ as well as a set of generalized Israel-Stewart equations from kinetic theory via Grad's 14-momentum expansion, which have several new terms.⁵⁵⁾ On the other hand, however, a stable first-order relativistic dissipative hydrodynamical scheme was also proposed on the basis of renormalization-group consideration.^{56), 57)}

In heavy ion physics, the shear viscosity, in particular its ratio with the entropy density, η/s , has been attracted most of the attention among the above three transport constants. Interesting seminal investigations on the effects of bulk viscosity have begun,^{58), 59)} while heat conductivity still has not been investigated systematically in connection with RHIC data. As for the second order parameters, there has been only little systematic investigations, either.

Once equations of state are given, Eq. (3.1) is solved, the effect of the phase transition being automatically taken into account, which is one of the advantages of the hydrodynamical model. We will discuss this feature in the next subsection. Recently the lattice(-inspired) equation of state which is connected to equation of state of resonance gas at low temperature is mostly used in hydrodynamical models. As the fireball expands, the temperature and density inside become so small that the assumption of the hydrodynamical picture becomes inapplicable any more. Thus, models with only a hydrodynamical component cannot describe the whole stages of the relativistic heavy ion collisions from the thermalized quark-gluon plasma stage to the kinetic freezeout. One way for such description is to connect a hydrodynamical simulation to a hadron based event generator as discussed in Sec. 6.

3.2. Equation of State and Transport Coefficients

One of the advantages of hydrodynamical models over other phenomenological models is their direct relation with the equation of state of QCD. Using the hydrodynamical models one can find directly the consequence of the phase transition in experimental observables. In hydrodynamical models, historically, the equation of state with a first order phase transition based on the bag model widely has been used, because of its simplicity and lack of conclusive results on the equation of state of QCD. In recent hydrodynamical calculations, lattice(-inspired) equation of state has been widely employed, because of the development of thermodynamical analyses based on the first principle calculation, lattice QCD simulation. The equation of state of QCD for 2+1 flavors and also that including charm quark (2+1+1 flavors) by means of lattice simulations were reported by Borsanyi et al.⁶⁰⁾ HoTQCD collaboration investigates chiral and deconfinement aspects of the phase transition with 2+1 flavors using several kinds of staggered fermions.⁶¹⁾ There was some difference between the two groups in the critical temperature, the temperature dependence of the so-called interaction measure and so on, but gradually the difference is disappearing. At the same time Wilson fermion simulation is also applied to the analysis of QCD thermodynamical properties.⁶²⁾ Quantitative analyses of the QCD thermodynamics with the lattice simulation have just started. For conclusive results, improvement in actions, approach to continuum limit, simulation at the real pion mass and so on

need to be done.

Simulations at finite chemical potential on the lattice suffer difficulty in execution of Monte Carlo simulations owing to the sign problem in the fermion determinant. Although there have been some developments recently such as the Taylor expansion method and reweighting method,^{(63),(64),(65),(66),(67),(68),(69),(70),(71),(72),(73)} the development in the study of finite chemical potential lattice simulations is relatively slow compared to lattice QCD study at the vanishing chemical potential. Though a lot of attempts to circumvent the problem have been made, we still need a breakthrough to explore the QCD properties in the whole region on the T - μ plane.

In relativistic viscous hydrodynamical models, we need to input more information related to transport coefficients, shear and bulk viscosities, heat conductivity, and relaxation times, besides equations of state. The investigation of the transport coefficients of strongly interacting QGP and hadron gas is one of the most difficult problems in the field. There are several studies on transport coefficients with various approaches; AdS/CFT,⁽⁵⁴⁾ lattice QCD,^{(74),(75)} finite temperature perturbative QCD,^{(76),(77),(78)} microscopic transport models,^{(79),(80),(81),(82),(83)} and relativistic quantum Boltzmann approach.⁽⁸⁴⁾ However, to reach a conclusive result on the transport coefficients, in addition to theoretical calculations, it plays an important role to extract transport coefficients from comparison of phenomenological model analyses and experimental data.

3.3. Jet Energy Loss

One of the most interesting features that are related to hydrodynamical expansion is the jet energy loss. A lot of interesting experimental results which suggest the existence of very large jet energy loss are reported. To explain these results interaction between jets and medium need to be understood. At the moment, there are perturbative QCD based approaches, the higher twist formalism, the AMY formalism, the GLV formalism, and ASW formalism, and AdS/QCD approach for the jet energy loss (References are found, for example, in Ref.⁽⁸⁵⁾).

Despite the large amount of effort put into the development of perturbative description of the hadron production in heavy ion collisions, there are uncertainties remaining about the exact nature of jet-medium interactions in the kinematic and temperature regimes relevant at RHIC. As a whole, the above four approaches describe RHIC data well, but they reach very different quantitative conclusions about the quenching strength, or transport coefficient, \hat{q} . This does not come as a big surprise since the approaches differ in some of their basic assumptions, and there are large uncertainties in modeling hard probes beyond the calculation of the energy loss rate for a quark or gluon.

Currently the big picture can be summarized as follows: perturbative calculations under various assumptions are compatible with RHIC data, but the constraints are insufficient to rule out any of the models. The experimental constraints are also insufficient to completely exclude non-perturbative mechanisms for jet quenching. Calculations using the AdS/CFT correspondence to model strongly interacting QCD^{(86),(87),(88)} can describe the same basic phenomenology. Most likely this challenge to perturbative QCD can only be answered at LHC. The extrapolation of jet quench-

Table III. pQCD-based energy loss models:⁸⁵⁾ This table summarizes some of the key assumptions of the four perturbative calculations discussed in the text. The models differ in the assumption on the medium (thermalized, perturbative), kinematics, scales (E = energy of the parton, k_T = transverse momentum of the emitted gluon, μ = typical transverse momentum picked up from the medium, T = temperature, Λ = typical momentum scale of the (non-thermalized) medium, x = typical momentum fraction of the emitted gluon), and the treatment of the resummation.

Model	Assumption about the medium and kinematics	Scales	Resummation
GLV	static scattering centers (Yukawa), opacity expansion	$E \gg k_T \sim \mu, x \ll 1$	Poisson
ASW	static scattering centers, multiple soft scattering (harmonic oscillator approximation)	$E \gg k_T \sim \mu, x \ll 1$	Poisson
HT	observable matrix elements at scale Λ (thermalized or non-thermalized medium)	$E \gg k_T \gg \Lambda \sim \mu$	DGLAP
AMY	perturbative, thermal, $g \ll 1$ (asymptotically large T)	$E > T \gg gT \sim \mu$	Fokker-Planck

ing to larger jet energies is significantly different in strong coupling and perturbative scenarios.⁸⁹⁾ It is also possible to assume a small regime of strong non-perturbative quenching around T_c together with the perturbative quenching at higher temperatures. Such hybrid scenarios might be hard to distinguish experimentally. One of such pictures was recently explored by Liao and Shuryak.⁹⁰⁾ They found that a “shell”-like quenching profile in which quenching is enhanced around T_c can give better simultaneous fits to single hadron suppression and elliptic flow. For more details, see, for example, Ref.⁸⁵⁾

3.4. Hydrodynamical Expansion

Before going to the discussion of experimental data on hydrodynamical expansion, in this subsection, we show the behavior of the temperature and chemical potential in hydrodynamical expansion. As an example, we depict the behavior of isentropic trajectories in the $T - \mu$ plane for Au+Au $\sqrt{s_{NN}} = 200$ GeV central collisions in Fig. 4. The dotted line stands for the phase boundary between the QGP and the hadronic phase (Note that due to small baryochemical potentials, the phase boundary is an almost flat line at $T_c = 160$ MeV). In addition to the central cell, we also investigate the isentropic trajectory of a cell close to the surface of the initially produced QGP. Whereas the isentropic trajectory of the central cell located at $(0, 0, 0)$ starts in the QGP phase (solid line), the cell at the initial surface of the QGP (dashed line) only exhibits an evolution from the mixed phase to the hadronic phase. Both trajectories are terminated at the freezeout temperature, $T_f = 110$ MeV.

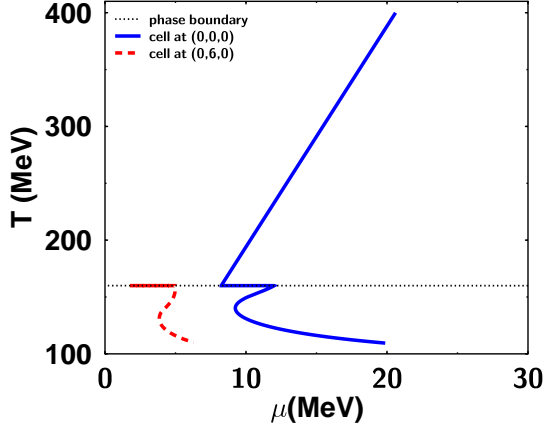


Fig. 4. Isentropic trajectories on the $T-\mu$ plane in the case of the 1st order phase transition. Solid (dashed) line stands for the time evolution of the cell which is located at $(x, y, \eta) = (0, 0, 0) (= (0, 6, 0))$ at the initial time. The dotted line represents the phase boundary.

3.5. Experimental Data and Discussion

Calculated results shown in this subsection are based on Ref.⁸⁾ To emphasize the importance of the final state interactions in the freezeout process in understanding hadron observables in relativistic heavy ion collisions, in this subsection we only show results of pure hydrodynamical calculation. The calculation is performed with a (3+1) dimensional ideal hydrodynamical model with the Glauber type initial condition and a bag model equation of state. Effects of final state interactions will be discussed in Sec. 6. This calculation, thus, can be considered as a baseline for recent more realistic hydrodynamical models.

In the initial energy density distribution, the maximum value of the energy density is 55 GeV/fm³, which is relatively higher than in other hydrodynamical models, because in the pure hydrodynamical calculation we just use a single freezeout temperature and neglect both resonance decays and final state interactions. Usually parameters for the initial condition are set from comparison with experimental data of single particle distributions, rapidity distributions and P_T distributions in central collisions. Therefore hydrodynamical models have prediction power for other physical observables such as collective flow and the impact parameter dependence of various physical observables. We include the small baryon number density in these calculations. The starting time of hydrodynamical expansion is $\tau_0 = 0.6$ fm. For the details of the parameters used in the calculations and the equation of state, see Ref.⁸⁾

First we show two examples which clearly show the limitation of pure hydrodynamical models. One is the P_T spectra of p and multistrange particles and the other is the elliptic flow as a function of the rapidity. Figure 5 shows the P_T spectra of π , K , and p in Au + Au at $\sqrt{s_{NN}} = 200$ GeV for central collisions. Our calculation succeeds in reproducing the π spectra measured by PHENIX⁹¹⁾ up to $P_T \sim 2$ GeV. However, due to the model assumption of chemical equilibrium down to the (low) kinetic freezeout temperature, we fail to obtain the correct normalization and hadron number ratios, even though the shape of the P_T spectra of p and multistrange

baryons (shown in Fig. 6) is close to that of the experimental data. In order to obtain the proper normalization for the p spectra and hadron number ratios, we adopt a procedure outlined in Ref.;⁹²⁾ it renormalizes the proton P_T spectra using the p to π ratio at the critical temperature. It is straightforward to extend this procedure to hyperons and multi-strange baryons as well, even though we choose to show the raw, unrenormalized, result for the multi-strange baryons in Fig. 6 to elucidate the situation prior to the renormalization.

The need for renormalizing the p spectra suggests that the assumption of a persistent chemical equilibrium throughout the hadron phase until kinetic freezeout is not realistic and that an improved treatment of the freezeout process is required. One method to deal with the separation of chemical and thermal freezeout is the *partial chemical equilibrium model (PCE)*.^{24),94),27)} below the chemical freezeout temperature T_{ch} one introduces a chemical potential for each hadron whose yield is supposed to be frozen out at that temperature. While the PCE approach can account for the proper normalization of the spectra, it fails to reproduce the transverse momentum spectra and mass dependence of the elliptic flow.⁹⁵⁾ In Sec. 6, we shall utilize our hybrid hydro+micro model to decouple the chemical freezeout from the kinetic freezeout. In these hybrid approaches,^{96),97),4)} the freezeouts occur sequentially as a result of the microscopic evolution. Flavor degrees of freedom are treated explicitly through the hadronic cross sections in the microscopic transport, which leads to the proper normalization of all hadron spectra.

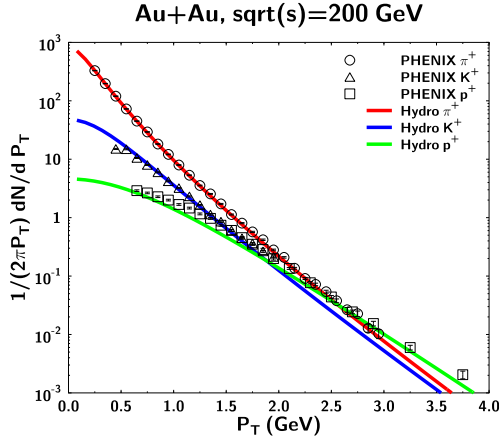


Fig. 5. P_T spectra for π^+ , K^+ , and p in central collisions with PHENIX data.⁹¹⁾ For the proton we rescale our result using the ratio at the chemical freezeout temperature. See the text.

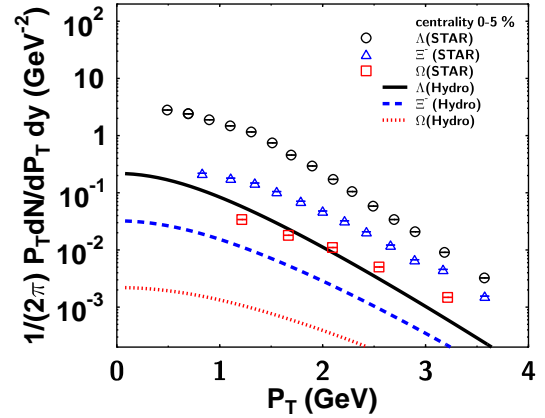


Fig. 6. P_T spectra for multi-strange baryons in central collisions with STAR data.⁹³⁾ In this pure hydro calculation no additional procedure for normalization has been done.

Figure 7 shows the elliptic flow as a function of the pseudo-rapidity η in central (3-15 %) and mid central collisions (15-25 %). In both cases our hydrodynamical model calculations overestimate the elliptic flow at forward and backward pseudo-rapidities, similarly to the results shown in Ref.²⁴⁾ At large forward and backward

rapidities the assumptions of perfect hydrodynamical models such as local equilibrium, vanishing mean free path, and negligible viscosity effect, are apparently no longer valid. The difference between experimental data and calculated results at forward and backward rapidities increases with the impact parameter, implying decrease of the volume in which the hydrodynamical limit is achieved.

Next we move on to the topic of jet energy loss in expanding hydrodynamical medium as one of interesting applications of hydrodynamical model. Figure 8 shows results from a comparative study by Bass et al. at RHIC.¹⁰⁰⁾ Jets are propagated through a medium described by the same hydrodynamics, using three different schemes for energy loss: ASW, Higher Twist (HT), and AMY. In Fig. 8 R_{AA} as a function of P_T for two different centrality bins is shown. It shows that the P_T -dependence and the centrality dependence of R_{AA} are described well by all three models. Each model has one free parameter that has been adjusted: the strong coupling α_S in AMY, \hat{q}_0 for the overall fit parameter in HT, K ($\hat{q} = K \cdot 2 \cdot \epsilon^{3/4}$) in ASW. These parameters are fixed from the comparison with R_{AA} data in central collisions (the top figure in Fig.8).

This study confirms the remarkably large \hat{q} in the ASW model compared to that in the HT approach. For the case where the quenching strength scales with $\epsilon^{3/4}$ the initial values $\hat{q}_0^{(*)}$ found for the quark at the center of the fireball in a central collision are¹⁰⁰⁾

$$\hat{q}_0 = 18.5 \text{ GeV}^2/\text{fm for ASW}, \quad \hat{q}_0 = 4.5 \text{ GeV}^2/\text{fm for HT} \quad (3.9)$$

and for the case where the quenching strength scales like the temperature T they are

$$\hat{q}_0 = 10 \text{ GeV}^2/\text{fm for ASW}, \quad \hat{q}_0 = 2.3 \text{ GeV}^2/\text{fm for HT}, \quad \hat{q}_0 = 4.1 \text{ GeV}^2/\text{fm for AMY}. \quad (3.10)$$

Note that the jet propagation in AMY model is calculated self-consistently as a function of the local temperature so that there is no difference between the two cases.

This comparison is unique and very valuable in the respect that the same initial hard cross sections and the same maps for the fireball, from the same (3+1)-dimensional ideal hydrodynamics were used. Any differences in the extracted values of \hat{q} are solely due to differences in models for the jet energy loss. One of the conclusions is that our current knowledge applied to R_{AA} leaves rather large uncertainty in the determination of \hat{q} .

Here we make a short comment on the jet energy loss at LHC. ALICE collaboration reported the nuclear modification factors R_{AA} as a function of P_T of charged particles in central and peripheral Pb-Pb collisions at $\sqrt{s_{NN}} = 2.76 \text{ TeV}$.¹⁰¹⁾ They found that in central collision R_{AA} is more suppressed up to $P_T = 7 \text{ GeV}$ compared to the PHENIX and STAR experiments at RHIC, which suggests that a much denser medium is produced and stronger parton energy loss occurs at LHC. R_{AA} decreases with P_T for $2 < P_T < 7 \text{ GeV}$ and it takes the minimum around $P_T = 7 \text{ GeV}$ and

^{*)} Note that the meaning of \hat{q}_0 in Eqs. (3.9) and (3.10) is different from the overall parameter \hat{q}_0 in HT. Both \hat{q}_0 are commonly used in the literature.

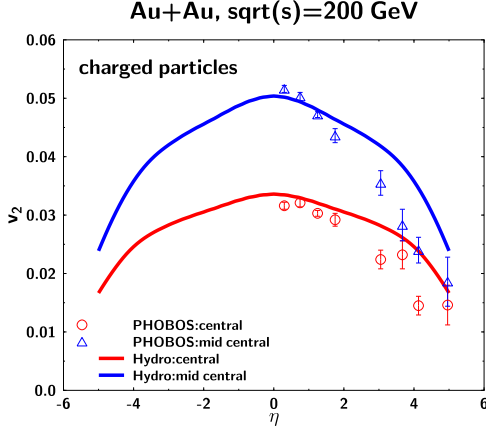


Fig. 7. Elliptic flow as a function of η with PHOBOS experimental data⁹⁸ for central (3-15 %) and mid central (15-25%) collisions. Impact parameters are set to 4.5 (central) and 6.3 (mid central) fm, respectively.

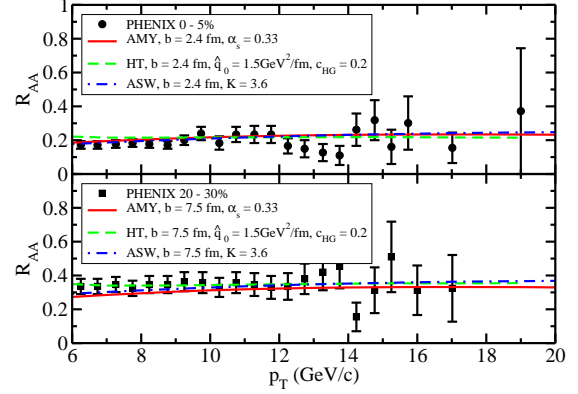


Fig. 8. R_{AA} as a function of P_T for central (top) and mid-central (bottom) collisions calculated from ASW, Higher Twist, and AMY energy loss models. The single parameter in each model has been fitted to describe the data by PHENIX.⁹⁹

interestingly, increases with P_T for $P_T > 7$ GeV. The increase of R_{AA} at high P_T was observed, for the first time, at LHC. It was not seen clearly at RHIC.

§4. Numerical Schemes for Solving Hydrodynamical Equations

In this section, we first explain the current status of hydrodynamical models from the point of view of numerical schemes for relativistic hydrodynamical equations. As we showed in Tabs. I and II, hydrodynamical models are categorized into ideal and viscous hydrodynamical models. In addition, the difference of each hydrodynamical model is found in the space-time dimension of simulation, initial conditions, equations of state, and prescriptions for freezeout process. In current understanding, the most realistic hydrodynamical model should have the following features: viscosity effects, (3+1) dimensional space-time expansion, event-by-event fluctuated initial conditions, lattice QCD inspired equations of state, and freezeout process which is described by hadron based cascade models. On these issues ideal hydrodynamical models have been studied more deeply and its status is considered to be more mature than viscous hydrodynamical models. The investigation with viscous hydrodynamical models has just started.

In addition to the above issues, an important ingredient in hydrodynamical models should be taken into account seriously. It is what numerical scheme is adopted for solving the relativistic hydrodynamical equation. Up to now, only a little attention has been paid to this point. As long as we analyze multiplicities and collective flow using smoothed initial conditions, which numerical scheme to choose is not so important. However, when we start to investigate viscosity effects and event-by-event fluctuations, we need to choose suitable numerical schemes carefully.

The relativistic hydrodynamical equation is a non-linear system equation, whose analytical solution is usually difficult to find. However, from the one dimensional wave equation $\partial_t u + c\partial_x u = 0$, which is much simpler than the actual relativistic hydrodynamical equation, we can explore a suitable numerical scheme by comparing with the analytical solution. The naive differential scheme such as the FTCS (Forward-Time Central-Space) scheme ($u_j^{n+1} = u_j^n - \frac{1}{2}\nu(u_{j+1}^n - u_{j-1}^n)$ ^{*)}, with $\nu = c\frac{\Delta t}{\Delta x}$) causes an unphysical oscillation, which continues to grow after several time steps. In order to stabilize the unphysical oscillation in the FTCS scheme, one can use, for example, the Lax-Friedrich scheme. In this scheme u_j^n on the right hand side of the FTCS scheme is replaced by the averaged value $\frac{1}{2}(u_{j-1}^n + u_{j+1}^n)$. This scheme is stable if the Courant-Friedrichs-Lewy condition (CFL condition) ($|\nu| < 1$) is satisfied, but it is known that it suffers huge numerical dissipation. In other words, the average manipulation introduces the artificial viscosity. One of the improved versions of Lax-Friedrich scheme is the Lax-Wendroff scheme, which has the second order accuracy in time and space,

$$\begin{aligned} u_{j+1/2}^{n+1/2} &= \frac{u_{j+1}^n + u_j^n}{2} - \frac{1}{2}c\frac{\Delta t}{\Delta x}(u_{j+1}^n - u_j^n), \\ u_j^{n+1} &= u_j^n - c\frac{\Delta t}{\Delta x}(u_{j+1/2}^{n+1/2} - u_{j-1/2}^{n+1/2}). \end{aligned}$$

This scheme is stable, but the unphysical oscillation occurs at discontinuity. In order to avoid this problem introduction of artificial viscosity or flux limitation is needed. In conjunction with this fact we just cite Godunov's theorem: no second-order or higher order explicit monotonous scheme exists. Systematic discussion on numerical schemes is out of scope of this article. For details, please see, for example, Ref.¹⁰²⁾ From these lessons for numerical schemes for the wave equation, we can deduce those for the relativistic hydrodynamical equation, though actual numerical tests are indispensable. i) First order accuracy scheme: For stability at discontinuity some average manipulation is needed, but this introduces large dissipation. ii) Second order accuracy: To remove numerical oscillation at discontinuity, one needs an artificial viscosity or a flux limiter. The former suggests that a simple central difference scheme of the first order accuracy might have a large artificial viscosity, which is crucial for the study of the viscosities of the matter created in relativistic heavy ion collisions.

For event-by-event fluctuated initial conditions, shock-wave capturing schemes play an important role in dealing with discontinuity in the initial conditions. A lot of shock-wave capturing schemes have been proposed and developed. On the other hand, in relativistic heavy ion collisions, SHASTA, rHLLE, and KT algorithms are mainly used. In particular, SHASTA algorithm, which is widely used in the study of relativistic heavy ion collisions, is known as the first version of Flux Corrected Transport (FCT) algorithm.¹⁰³⁾ In this algorithm, first a low-order solution is calculated. It incorporates large numerical diffusion effect. In the second step, as much

^{*)} The upper index (n) stands for the time step and the lower index (j) stands for the spacial position.

diffusion as possible is removed from the low-order solution. The amount of antidiffusion fluxes is determined with the mask coefficient A_{ad} . This default value is $A_{\text{ad}} = 1$, which can be set to lower values to reduce the amount of antidiffusion. In Ref.¹⁰⁴⁾ an interesting demonstration of the interplay between the numerical viscosity and physical viscosity was shown. A comparison was made with numerical solutions of the Riemann problem, one with the standard mask coefficient $A_{\text{ad}} = 1.0$ SHASTA with a small physical viscosity $\eta/s = 0.01$ and the other with a reduced mask coefficient $A_{\text{ad}} = 0.8$ SHASTA with vanishing viscosity. It was found that the difference of two numerical calculations is very small, which implies that it might be difficult to distinguish between the physical viscosity and the artificial dissipation. For quantitative investigation of the viscosities in the quark matter, one need to estimate the amount of artificial viscosity existing in numerical schemes carefully or choose numerical schemes known to have less artificial viscosity. Furthermore in Ref.,¹⁰⁴⁾ a comparison among the different shock-wave capturing schemes, SHASTA, KT, and NT schemes was made and found that all the algorithms reproduce the analytic solution with nearly the same accuracy and numerical artifact (Figs. 9 and 10).

Recently, Ref.¹⁰⁵⁾ proposed a fast numerical scheme for causal relativistic hydrodynamics with dissipation for analyses of relativistic high energy collisions, which is based on Ref.¹⁰⁶⁾ In the numerical scheme, Israel-Stewart theory was adopted and the Israel-Stewart equations were decomposed into the inviscid part and the dissipative part. For the inviscid part a relativistic Riemann solver^{108), 109), 110), 111), 112), 113), 114), 115), 116)} is used and for the dissipative part the Piecewise Exact Solution method¹¹⁷⁾ is employed in order to achieve less artificial dissipation and less computational time. Riemann solvers are numerical fluid dynamical solvers which are based on the concept of the Riemann problem. Several kinds of Riemann solvers have been proposed: Godunov method, Roe scheme, HLLE and HLLC solvers, and so on. Each solver has advantages and disadvantages in numerical cost, calculational accuracy, and coding complexity.^{102), 107)} In order to obtain the correct physical viscosity, for the inviscid part as well as the dissipative part, we need to choose numerical schemes which suffer as little artificial dissipative effect as possible. In Ref.,¹⁰⁵⁾ for the inviscid part they use the relativistic Godunov method which is based on the exact solution of the Riemann problem. Figures 9 and 10 show numerical solutions of the relativistic Riemann problem for ideal fluid on a grid with $N_x=100$ cells with $\Delta x=0.1$ fm after $N_t = 100$ time steps at $t = 4$ fm together with the analytic solution. The initial conditions are set as the same as those in Ref.¹⁰⁴⁾ On the left the initial temperature is $T_0 = 0.4$ GeV and on the right $T_0 = 0.2$ GeV, and the energy density ϵ is given by $\epsilon = \frac{3g}{\pi^2} T^4$ ($g = 16$). The numerical results for SHASTA, KT, and NT schemes are taken from Ref.¹⁰⁴⁾ SHASTA, KT, and NT schemes reproduce the analytic Riemann solution with nearly the same accuracy and numerical artifacts. On the other hand, we can see that the red line¹⁰⁵⁾ is closer to the analytical solution around $x = 3$ fm, which implies that this scheme suffers less artificial dissipative effect and is more suitable for physical viscosity analyses. A comparison of rHLLE and SHASTA was done in Ref.¹¹⁸⁾ It was found that rHLLE has almost the same artificial viscosity as

SHASTA.

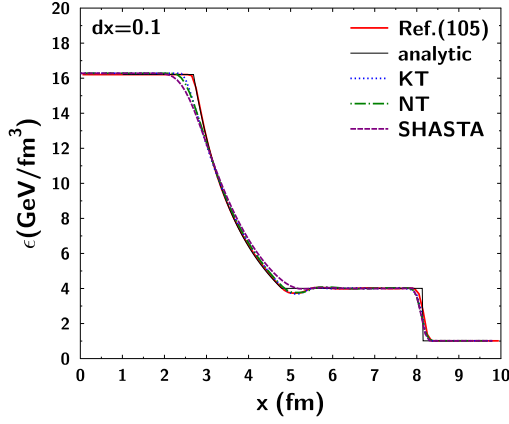


Fig. 9. Energy density distributions as a function of x from numerical results (SHASTA (short-dashed line), KT (dotted line), NT (long-dashed line), and Ref.¹⁰⁵⁾ (red solid line)) together with the analytic Riemann solution.

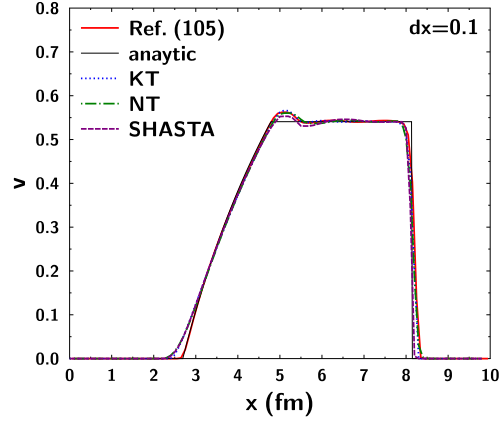


Fig. 10. Velocity distributions as a function of x from numerical results (SHASTA (short-dashed line), KT (dotted line), NT (long-dashed line), and Ref.¹⁰⁵⁾ (red solid line)) together with the analytic Riemann solution.

§5. Hadronization

In hydrodynamical models the hadronization process from the QGP phase to the hadron phase is naturally encoded in the equation of state. At RHIC hydrodynamical calculations do well for explaining a lot of experimental data, the P_T spectra, and the elliptic flow up to $P_T \sim 2$ GeV. However, above $P_T \sim 2$ GeV the results from hydrodynamical models start to show deviation from experimental data, which suggests that other mechanisms become dominant at higher P_T instead of the hydrodynamical feature. In the intermediate P_T ($2 \leq P_T \leq 6$ GeV) the recombination mechanism is dominant and at high P_T (≥ 6 GeV) the fragmentation mechanism plays an important role. These transverse momentum regions where the hydrodynamical picture, recombination model, or fragmentation mechanism works well depend on collision energy. For example, at LHC the hydrodynamical description may work up to $P_T \sim 4 - 5$ GeV.³⁴⁾ There have been attempts to use thermodynamical properties which are described with a hydrodynamical model as inputs of the recombination model and fragmentation mechanism.^{119),120)} It may become possible to construct more realistic dynamical models to understand the physics of relativistic heavy ion collisions by employing the recombination model and fragmentation process for hadronization in a hydrodynamical model. In the next subsection, we give a brief description of the recombination model.

5.1. Recombination Model

Quark recombination or coalescence is the best candidate for the physical mechanism to explain a large amount of experimental data at the intermediate P_T at

RHIC. Now not only at LHC but also at relatively low collisions energy experiments, analyses with the recombination picture are ongoing.¹²¹⁾ First the quark number scaling law was found in the behavior of elliptic flow as a function of the transverse momentum, which is considered as a signature of the quark recombination. For a quark phase with the elliptic flow $v_2^q(P_T)$ at the time of the hadronization simple instantaneous recombination models predict

$$v_2^H(P_T) = n v_2^q \left(\frac{P_T}{n} \right), \quad (5.1)$$

where n is the number of the valence quarks. This scaling law describes the key feature of experimental data at the intermediate P_T notably well.

Generally, recombination models assume a universal phase space distribution of quarks at hadronization. Quarks turn into baryons, $qqq \rightarrow B$, and mesons, $q\bar{q} \rightarrow M$. These processes are described either by using instantaneous projections of quark states onto hadron states,^{122), 123), 124), 125), 126)} or dynamical coalescence processes with finite width hadrons governed by rate equations.¹²⁷⁾ Note that usually only the valence quarks of the hadron are taken into account although generalization has been attempted.¹²⁶⁾

The original instantaneous projection models explicitly preserve only three components of the energy-momentum four-vector in the $2 \rightarrow 1$ and $3 \rightarrow 1$ processes. The yield of mesons can be expressed through the convolution of the Wigner function W_{ab} for a pair of partons, a and b and the Wigner function Φ_M encoding the meson wave function

$$\frac{dN_M}{d^3P} = \int \frac{d^3R}{(2\pi)^3} \sum_{ab} \int \frac{d^3q d^3r}{(2\pi)^3} W_{ab} \left(\mathbf{R} + \frac{\mathbf{r}}{2}, \frac{\mathbf{P}}{2} + \mathbf{q}; \mathbf{R} - \frac{\mathbf{r}}{2}, \frac{\mathbf{P}}{2} - \mathbf{q} \right) \Phi_M(\mathbf{r}, \mathbf{q}). \quad (5.2)$$

The quark Wigner functions are usually approximated by the classical phase space distributions. Hadron spectra at intermediate P_T are described well by considering the factorization of W_{ab} into the thermal quark distributions,¹²³⁾

$$W_{ab}(\mathbf{r}_1, \mathbf{p}_1; \mathbf{r}_2, \mathbf{p}_2) = f_a(\mathbf{r}_1, \mathbf{p}_1) f_b(\mathbf{r}_2, \mathbf{p}_2). \quad (5.3)$$

Correlations between quarks can be introduced to model correlations found between hadrons¹²⁸⁾ without interfering with the excellent description of the spectra and hadron ratios.

The strength of the quark recombination picture is in its predictive power, which originates from its explaining all measured hadron spectra at the intermediate P_T basically with one parameter for the quark distribution function at hadronization. It has been shown that at low momenta resonance recombination is compatible with hydrodynamics and kinetic equilibrium,¹²⁹⁾ but on the other hand, because thermalized states do not retain memories of previous time, all phenomena with long time scale in the equilibrated region should be expected to be described by hydrodynamics. They include the quark number and kinetic energy scaling observed at RHIC at low momenta.¹²⁹⁾ The possibility of including quark recombination explicitly into hydrodynamical model has been studied in Refs.^{119), 120)}

5.2. Experimental Data and Discussion

Using the recombination model, we can explore the production of quark soup, which is a consequence of the QCD phase transition. After the success of the recombination model at RHIC, the scaling property of the elliptic flow has been tested in a wide range of collision energy to investigate the properties of the strongly interacting QGP. The elliptic flows of π^\pm , p , and Λ were measured in Pb+Pb collisions at $\sqrt{s_{NN}} = 17$ GeV at SPS by NA49.¹³⁰⁾ They found that the quark number scaling in the elliptic flows of these particles holds in the P_T range covered by the data (up to $P_T/n \approx 1$ GeV. Fig. 6 in Ref.¹³⁰⁾). Since the P_T is limited to rather low values, however, this should not be viewed as a conclusive test for the quark recombination mechanism at SPS.

At LHC the analyses of the quark number scaling in the elliptic and triangular flows of identified particles have just started. In Ref.,¹³¹⁾ ALICE shows the elliptic and triangular flows per constituent quark of π^\pm , K^\pm , and \bar{p} as a function of the transverse kinetic energy (KE_T) per quark for more central (10 -20 %) and more peripheral (40-50 %) Pb+Pb collisions at $\sqrt{s_{NN}} = 2.76$ TeV. They report that within errors the flows of π and K follow the scaling, while the flow of \bar{p} deviates in the more central and more peripheral events. In the triangular flow they find the same feature as the elliptic flow, i.e., the triangular flow of \bar{p} shows deviations from the KE_T scaling. However, this investigation is done in a relatively low transverse kinetic energy region ($KE_T/n < 1$ GeV) where the hydrodynamical behavior is expected to be dominant. Therefore, this deviation from the KE_T scaling in the elliptic and triangular flows could be explained by the mass splitting and mass ordering realized by hydrodynamical motion. To obtain a conclusive result for the quark number scaling in the collective flow at LHC measurement at higher transverse kinetic energy, where the effects of the recombination mechanism are more clearly observed, is indispensable.

For the experimental confirmation of the quark number scaling in the elliptic flow, no particles are more important than the ϕ meson. Because it is composed of one quark and one antiquark and its mass is close to that of the proton, analyses of the elliptic flow of ϕ reveal the dominant process in the hadronization at the intermediate P_T : recombination mechanism or thermal process as described by hydrodynamics.¹³²⁾ In addition, because multi-strange hadrons have large mass and small hadronic cross sections, they should be less sensitive to hadronic rescattering in the later stage of collisions and a good probe of the early state of the collisions such as the partonic elliptic flow. STAR Collaboration measured the v_2 of multi-strange hadrons (ϕ , Ξ , and Ω) in Au+Au collisions at $\sqrt{s_{NN}} = 200$ GeV and showed the quark number scaling works in the elliptic flow of the multi-strange hadrons.¹³³⁾ This implies that the partonic collectivity is built up at the top RHIC energy.

Furthermore STAR Collaboration investigates the energy dependence of the elliptic flow as a function of the transverse momentum for ϕ at RHIC.¹³⁴⁾ The quark number scaling in the elliptic flows of π , K , p , Λ , and Ξ works well at both $\sqrt{s_{NN}} = 39$ and 11.5 GeV in Au+Au collisions. They found that while at $\sqrt{s_{NN}} = 39$ GeV the elliptic flow of ϕ also follows the quark number scaling, at

$\sqrt{s_{NN}} = 11.5$ GeV the elliptic flow per constituent quark of ϕ is much smaller than those of the other particles. Only the ϕ meson is out of the quark number scaling of the elliptic flow at this energy. They conclude that it indicates the dominance of hadronic interactions with the decrease of the beam energy. To confirm this, measurement of the elliptic flow of Ω would be helpful.

At the top RHIC energy, the elliptic flow of hadrons which contain only light flavor quarks (u , d , and s) follows the quark number scaling. Does the quark number scaling work in the elliptic flow of hadrons which are composed of heavy flavors? Recent STAR measurement of the elliptic flow of J/ψ gives the answer to this question. It shows that the elliptic flow of J/ψ is consistent with zero over the measured P_T range, which is significantly smaller than that of ϕ and inclusive charged hadrons.¹³⁵⁾ The picture that J/ψ production is dominated by charm quark recombination with significant charm quark flow is disfavored. On the other hand, the elliptic flow of open charm mesons is well understood by the recombination of a light (anti)quark and an (anti)charm quark with elliptic flow.¹³⁶⁾

Next we argue that the recombination model is one of powerful tools to understand hadron properties and the QCD phase diagram with high energy heavy ion collisions. The investigation of the elliptic flow of hadron resonances with the recombination picture at RHIC makes it possible to know final state interactions in the freezeout processes and the structure of resonances.¹³⁷⁾ In principle, there are two different mechanisms that contribute to resonance production and as a result there are two types of resonances: (1) primordial resonances - resonances produced from hadronizing quark gluon plasma (QGP mechanism), and (2) secondary resonances - resonances produced in the hadronic final state via hadron-hadron scattering (HG mechanism). For example, in the case of K_0^* , which is composed of the d and \bar{s} quarks, K_0^* are produced by the recombination of the d and \bar{s} quarks in the QGP mechanism, while it is created via scattering of K and π in the HG mechanism. The recombination model tells us that the scaling constant n of the elliptic flow of a hadron species is given by the number of constituent quarks which participate in the production of the hadron: in the case of the QGP mechanism $n = 2$, and in the case of HG mechanism $n = 4$. From these two contributions the measured elliptic flow is given by,

$$v_2^{\text{measured}} = r(P_T)v_2^{\text{QGP}} + (1 - r(P_T))v_2^{\text{HG}}, \quad (5.4)$$

where $r(P_T)$ is the fraction of resonances which were produced at the hadronization and whose decay products escaped from the hadron phase without rescattering. With $r(P_T)$ one can investigate the cross sections of resonances in the hadronic medium. STAR attempted to extract the scaling constants (or apparent constituent quark number) from the measured elliptic flow of K^{0*} to investigate its production mechanism. Unfortunately, the obtained value of n is $n = 3 \pm 2$,¹³⁸⁾ from which we cannot draw a definite conclusion. This method is easily extended to explore the structure of exotic hadrons, such as tetraquark and pentaquark. Utilizing the scaling law of the elliptic flow, one can obtain the information on the structure of exotic hadrons, whether they have compact structure or are more like molecular bound states.¹³⁷⁾

We can explore consequences of diquark and quark-antiquark clustering above the deconfinement temperature with event-by-event net charge fluctuations.¹³⁹⁾ Recently, lattice QCD calculations show that charmonia survive even well above the critical temperature,^{140),141),142),143)} which suggests the possibility that hadronization occurs via recombination of not only single q or \bar{q} but also qq or $q\bar{q}$. The D measure, the net charge fluctuation normalized by the entropy is defined by

$$D = 4\langle(\Delta Q)^2\rangle/N_{\text{ch}}, \quad (5.5)$$

where $\langle(\Delta Q)^2\rangle$ denotes the event-by-event net charge fluctuation within a given rapidity window Δy and N_{ch} is the total number of charged particles emitted in this window. For a free plasma of quarks and gluons $D \approx 1$, whereas for a free pion gas $D \approx 4$. However, experimental data at RHIC is rather close to the value of hadron gas $D = 2.8 \pm 0.05$ in central Au+Au collisions at $\sqrt{s_{NN}} = 130$ GeV (STAR)¹⁴⁴⁾ and $D \approx 3$ (PHENIX).¹⁴⁵⁾ In the recombination scenario, the fluctuation of the net charge $Q = \sum_i q_i n_i$ is given as

$$\langle\delta Q^2\rangle \equiv \langle Q^2\rangle - \langle Q\rangle^2 = \sum_i (q_i)^2 \langle n_i\rangle + \sum_{i,k} c_{ik}^{(2)} \langle n_i\rangle \langle n_k\rangle q_i q_k, \quad (5.6)$$

where $c_{ik}^{(2)}$ are the normalized two-particle correlation functions. In the absence of two-particle correlations, Eq. (5.6) can be rewritten as $\langle\delta Q^2\rangle = \frac{4}{9}(N_u + N_{\bar{u}}) + \frac{1}{9}(N_d + N_{\bar{d}} + N_s + N_{\bar{s}})$, where $N_i = \langle n_i\rangle$ denotes the average number of the constituent quarks with flavor i . Together with the statistical hadronization model and the multiplicity of experimental value, the net charge fluctuation in the quark recombination scenario is $d\langle\delta Q^2\rangle_q/dy = 331 \pm 27$, which is close to the experimental value $d\langle\delta Q^2\rangle_{\text{had}}/dy = 368 \pm 33$.¹⁴⁴⁾ Furthermore the difference of the net charge fluctuations between the quark recombination and the experimental data suggests necessity of improvement on both theory and experiment sides. One of such possibilities is to include qq and $q\bar{q}$ pairs to the hadronization mechanism.¹³⁹⁾ If the qq pair and $q\bar{q}$ are taken into account, Eq. (5.6) is extended to

$$\langle\delta Q^2\rangle = \sum_i (q_i)^2 (N_i + N_{\bar{i}}) + \sum_{ij} (q_i + q_j)^2 \langle n_{ij}\rangle + \sum_{ij} (q_i - q_j)^2 \langle \bar{n}_{ij}\rangle, \quad (5.7)$$

where the average numbers of diquarks and $q\bar{q}$ are proportional to the products of the individual quark numbers: $\langle n_{ij}\rangle = \alpha(N_i N_j + N_{\bar{i}} N_{\bar{j}})$, $\langle \bar{n}_{ij}\rangle = \beta N_i N_{\bar{j}}$ with relative pairing weights α and β . They showed that experimental data can be fitted with an appropriate choice of α and β .

In Ref.,¹³⁹⁾ the problem of the gluonic degrees of freedom was also discussed. According to recent lattice calculations,^{60),61),62)} the phase transition at small baryon chemical potential is crossover. This means that the hadronization at RHIC and LHC does not take place from a system where quarks and gluons are active degrees of freedom, but from a state with reduced entropy density. At the moment, no method on the lattice has been found to figure out what is the active degrees of freedom in the crossover region. In Ref.¹³⁹⁾ it was shown that entropy density data on the lattice

are not inconsistent with that of a gas of constituent quarks, which is assumed in the recombination model. The success of the recombination model strongly suggests that the gluonic degrees of freedom disappear first when the temperature is decreased from well-above the (pseudo)critical temperature. However, it is needless to say that it is important to find a way to figure out how the active degrees of freedom change across the crossover region on the lattice in order to steady this picture.

§6. The Freezeout Process

As fireballs expand, the temperature and density inside them become small. Finally the mean free path among particles inside the fireballs becomes so large that the assumption for the hydrodynamical picture becomes invalid. Currently two separate freezeout processes are believed to occur successively in heavy ion collisions. One is chemical freezeout, at which the ratios of hadrons are fixed, and the other is thermal (kinetic) freezeout, at which the particles stop interacting. Recently final state interactions between the two freezeout processes are also included in hydrodynamical models by connecting hadron based event generators to the hydrodynamical calculations. In this picture, kinetic freezeout is found to be not an instantaneous process but a continuous one as we show in the following.

6.1. Chemical Freezeout and Thermal Freezeout

The chemical freezeout temperature and baryon chemical potential are extracted with the statistical model on the basis of the grand canonical formalism. Surprisingly, statistical models are in excellent agreement with experimental data for hadron ratios in a wide range of collision energy from SIS to RHIC.¹⁴⁶⁾ At present the (pseudo)critical temperature suggested from the latest lattice calculation is $T_c = 150 \sim 160$ MeV (see Subsec. 3.2), which is relatively low from the point of view of the statistical model.¹⁴⁷⁾ For example, using a statistical model, Andronic et al. extract the chemical freezeout temperature $T_{\text{ch}} = 160 \sim 166$ MeV for LHC Pb+Pb collisions at $\sqrt{s_{\text{NN}}} = 2.76$ GeV. It might be too early to take lattice results at the face value, but this suggests that the physical meaning of the temperature and chemical potential obtained by the statistical model need to be reexamined. At the same time, one needs to make it clear why the statistical model works very well not only in a wide range of collision energies from SIS to LHC but also for smaller systems such as $p+p$ collisions.¹⁴⁸⁾

At the thermal freezeout temperature, the mean free paths of the hadrons have grown to the order of the system size and hydrodynamical description, which requires very small mean-free path, is clearly no longer applicable. A first naive guess for the kinetic freezeout temperature T_f would be of the order of the pion mass (~ 140 MeV). Practically the value of the kinetic freezeout temperature in hydrodynamical models is determined from comparison with data of the P_T -spectra.

The task at the end of a hydrodynamical calculation is to populate fluid cells with particles with the final temperature and flow. For calculations of single particle spectra, the simple assumption of a sudden freezeout process at a certain proper time for each fluid cell is often adopted, neglecting the reverse process from particles to

the hydrodynamical medium. Under this assumption the Cooper-Frye formula¹⁴⁹⁾ is widely used,

$$E \frac{dN}{d^3P} = \sum_h \frac{g_h}{(2\pi)^3} \int_{\Sigma} d\sigma_{\mu} P^{\mu} \frac{1}{\exp[(P_{\nu} u^{\nu} - \mu_f)/T_f] \pm 1}, \quad (6.1)$$

where g_h is the degeneracy factor of hadron h and T_f and μ_f are the freezeout temperature and baryon chemical potential, respectively, and $+$ $(-)$ is for fermions (bosons). $d\sigma_{\mu}$ is obtained by calculating the normal vector on the freezeout hypersurface Σ . Once these quantities are given, using Eq. (6.1), one can calculate the distribution of any particle after freezeout.

More realistic models have been investigated. One of them is the Continuous Emission Model (CEM), in which particles are emitted continuously from the whole expanding volume of the system at different temperatures and different times.¹⁵⁰⁾ In the early days of hydrodynamics only kinetic freezeout was implemented. Indeed, at lower collision energies such as at SIS and AGS, the separation between the chemical freezeout and kinetic freezeout points is not large on the $T - \mu$ plane. However, at RHIC there is a significant difference between kinetic freezeout temperatures from hydro-inspired models and the chemical freezeout temperature from the statistical model.¹⁵¹⁾ This fact also manifests itself through the failure to get the correct absolute normalization of some P_T -spectra, e.g., that of protons in hydrodynamical calculations, with only a kinetic freezeout.¹⁵²⁾ For these reasons, attempts to model separate freezeout processes consistently via modified equations of state were started.^{24), 153), 154), 94)}

6.2. Final State Interactions

It turns out that some experimental data are still not understood in a satisfactory way even with the two separate freezeouts. For example, mean transverse momentum $\langle P_T \rangle$ as a function of particle mass does deviate from the linear scaling law, which suggests significant final state interactions in the hadronic phase.⁸⁾ To explain these effects, and to account for the apparently large viscosities in the hadronic phase, as discussed before, hydro+cascade hybrid models were introduced. They use a hydrodynamical computation of the expansion and cooling of hot QCD bulk matter, and then couple the output consistently to a hadron-based transport model in order to take account of the final state interactions. A pioneering work on hydro+cascade hybrid models was done by Bass et al.¹⁵⁵⁾ using UrQMD. Similar investigations were carried out in Refs.^{25), 4)} Figure 11 shows a schematic sketch of the hydro + UrQMD model.⁸⁾ At the switching temperature T_{SW} , the mean free path of hadrons becomes so large that the hydrodynamical picture becomes inapplicable. Thus after this point, the motion of hadrons is described by UrQMD. In practice, at T_{SW} hadron distributions are calculated with the Cooper-Frye formula in the fluid and the initial state of UrQMD is produced with them through the Monte Carlo methods. Then the UrQMD simulation is started. The reverse process from UrQMD to fluid dynamics is neglected in the simulation.

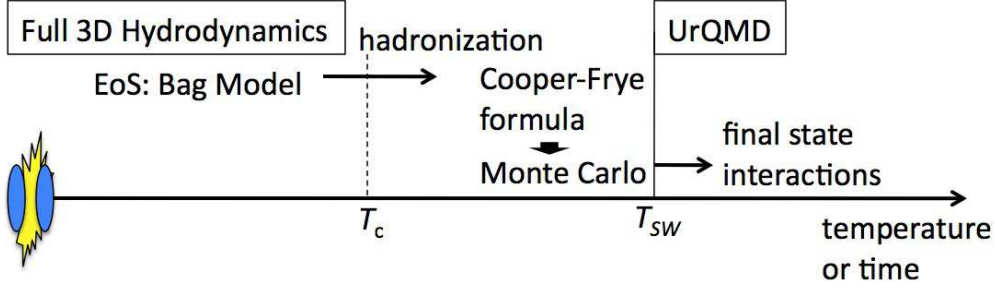


Fig. 11. Schematic sketch of the 3D hydro+UrQMD model. T_c and T_{sw} are taken to be 160 MeV and 150 MeV, respectively.

6.3. Experimental Data and Discussion

The main purpose of our hydrodynamical model + hadron based event generator is to handle realistic final state interactions in the freezeout process. We need to choose an appropriate hadron based event generator for it. Hadron based event generators have been developed to understand experimental data especially at lower energy heavy ion collisions. Here we use the UrQMD model for the description of final state interactions in the hadron phase. It gives us reasonable hadron yields, single particle spectra and so on, and it is often used for understanding the baseline of experimental data of relativistic heavy ion collisions.

Here we make a comment on the applicability of cascade models for the description of the afterburner of hydrodynamical models. Recent lattice calculations (Ref.⁶⁰) suggest that the hadron phase is well-described as a hadron resonance gas up to the vicinity of the phase transition. Thus, cascade models are, in general, ideal machinery to investigate its time evolution and freezeout process.

If the final state interactions are implemented properly, hydrodynamical models acquire more predictive power for experimental observables. We will show this by comparing single particle spectra and elliptic flows with experimental data. In this subsection we show results calculated with the same initial conditions and the equation of state as those in pure hydrodynamical calculations: Glauber type initial conditions and a bag model equation of state. In this case the maximum value of initial energy density is 40 GeV/fm³, which is smaller than that of the pure hydrodynamical model, because the inclusion of resonance decays and final state interactions to hydrodynamical models increases particle multiplicity.

First let us consider the argument on the multiplicity, which we mentioned in Sec. 2. We take π^+ as an example, because it is one of the most dominant particles in the charged hadron multiplicity and affected a lot from resonance decays. Figure 12 shows the pseudo rapidity distributions of π^+ from the fluid at T_{sw} (solid line), that from the fluid plus resonance decay effects (open circles), and its final state multiplicity (solid circles). We find that the resonance decay effect is huge and that the multiplicity including resonance decay effect (open circles) becomes almost twice as many as that of hydro at T_{sw} (solid line). Furthermore, the additional gain from final state interactions is seen. This result clearly shows that the dynamics of the

hadron phase such as resonance decays and final state interactions, is important also in high energy heavy ion collisions. In short, final state multiplicities cannot be predicted by determining only the initial state.

Figure 13 shows the P_T spectra of π^+ , K , and p in central collisions at $\sqrt{s_{NN}} = 200$ GeV. The most remarkable feature, compared to the pure hydrodynamical calculation, is that the hydro+micro approach is capable of accounting for the proper normalization of the spectra for all hadron species without any additional correction as is performed in the pure hydrodynamical model. The introduction of realistic freezeout process provides therefore a natural solution to the problem of the separation of the chemical and kinetic freezeouts in pure hydrodynamical calculation. Similar results have been obtained previously in 1+1 and 2+1 dimensional implementations of the hydro+micro approach.^{96),156)}

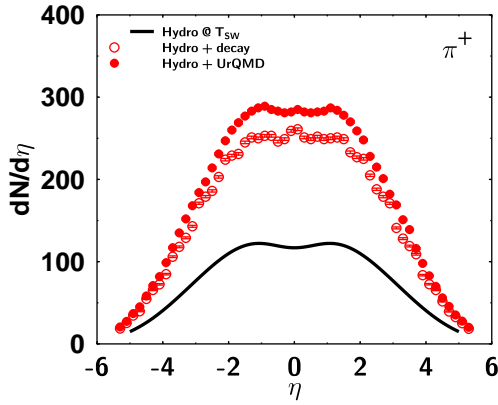


Fig. 12. Pseudo rapidity distribution of π^+ from hydro at T_{sw} (solid line), hydro + decay (open circle), and hydro + UrQMD (solid circle) in Au+Au $\sqrt{s_{NN}} = 200$ GeV central collisions.

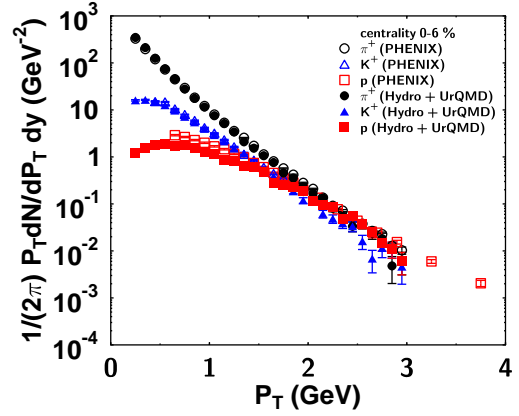


Fig. 13. Comparison of the calculated P_T spectra for π^+ , K^+ , and p in central collisions with PHENIX data.⁹¹⁾ The points are not renormalized.

In Fig. 14 we analyze the P_T spectra of multi-strange particles. Our results show good agreement with experimental data for Λ , Ξ , and Ω for centralities 0–5 % and 10–20 %. In this calculation no additional procedure for normalization is needed. Recent experimental results suggest that at the thermal freezeout multi-strange baryons exhibit less transverse flows and higher temperatures closer to the chemical freezeout temperature compared to non- or single-strange baryons.^{157),158)} This behavior can be understood in terms of the flavor dependence of the hadronic cross section, which decreases with increasing strangeness content of the hadron. The reduced cross section of multi-strange baryons leads to a decoupling from the hadronic medium at an earlier stage of the reaction, allowing them to provide information on the properties of the hadronizing QGP less distorted by hadronic final state interactions.^{159),160),156)} It should be noted that the analogous behavior has already been observed in experiments at CERN SPS.¹⁶¹⁾

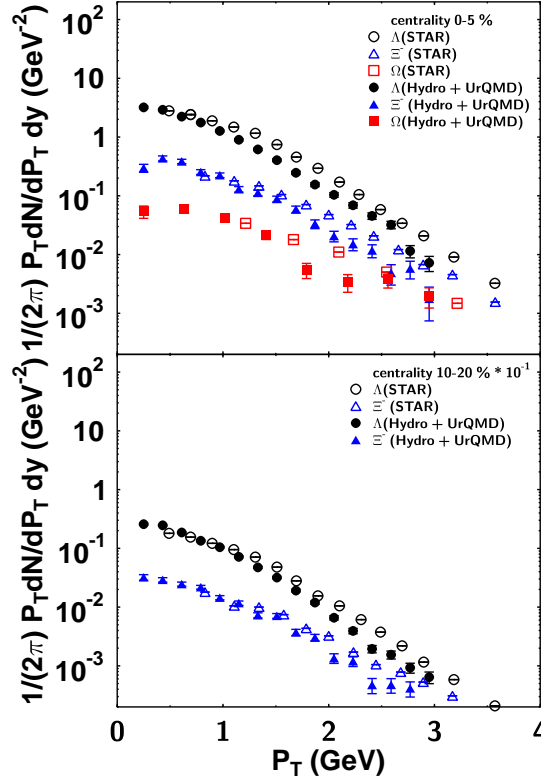


Fig. 14. Calculated P_T spectra of multi-strange particles at centralities 0–5 % and 10–20 % and STAR data.¹⁵⁷⁾

In Fig. 15 the mean transverse momentum $\langle P_T \rangle$ as a function of the hadron mass is shown. Open symbols denote the value at $T_{sw} = 150$ MeV, corrected for hadronic decays. Not surprisingly, in this case the $\langle P_T \rangle$ follows a straight line, suggesting a hydrodynamical expansion. However, if hadronic rescattering is taken into account (solid circles), the $\langle P_T \rangle$ does not follow the straight line any more. The $\langle P_T \rangle$ of pions is actually reduced by hadronic rescattering (they act as a heat-bath in the collective expansion), whereas protons actually pick up additional transverse momentum in the hadronic phase. RHIC data by STAR collaboration are shown by the solid triangles – overall, the proper treatment of hadronic final state interactions significantly improves the agreement of the model calculation with the data. We note that our results confirm those previously obtained in 1+1 and 2+1 dimensional implementations of the hydro+micro approach,^{96),156)} demonstrating the robustness of the hydro+micro approach across the three different implementations of the hydrodynamical and macro to micro transition components of the model.

Let us now investigate the effect of resonance decays and hadronic rescattering on the pion and baryon transverse momentum spectra. Figure 16 shows the P_T spectrum of π^+ at $T_{sw} = 150$ MeV (solid line, uncorrected for resonance decays)

as well as the final spectrum after hadronic rescattering and resonance decays, labeled as *Hydro+UrQMD* (solid symbols). In addition, the open symbols denote a calculation with the resonance decay correction performed at T_{sw} , which we label as *Hydro+decay*. The difference between the solid line and open symbols therefore directly quantifies the effect of resonance decays on the spectrum, which is most dominant in the low transverse momentum region $P_T < 1$ GeV. Furthermore, the comparison between the open symbols and solid symbols quantifies the effect of hadronic rescattering: pions with $P_T > 1$ GeV lose momenta via these final state interactions, resulting in the steeper slope.

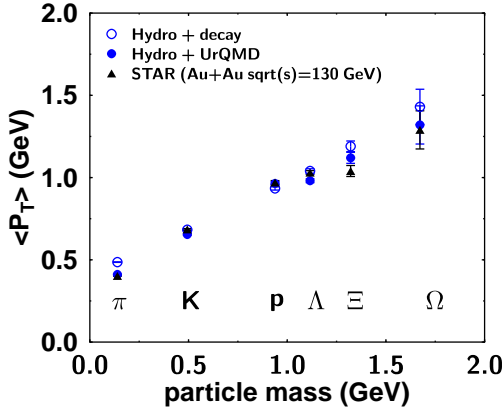


Fig. 15. Mean P_T as a function of mass. The open circle symbols stand for hydro + decay, solid circle symbols stand for hydro + UrQMD, and solid triangle symbols stand for STAR data (Au+Au $\sqrt{s_{NN}} = 130$ GeV).

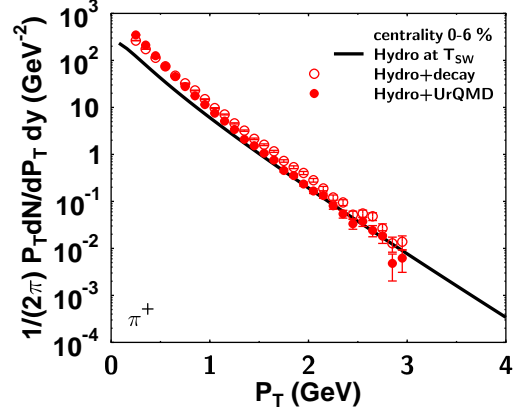


Fig. 16. P_T spectra of π^+ from hydro at the switching temperature (solid line), hydro+decay (open symbols) and hydro + UrQMD (solid symbols) in central collisions.

Figure 17 shows the elliptic flow as a function of η : the pure hydrodynamical calculation is shown by the solid curve, the hydrodynamical contribution at T_{sw} is denoted by the dashed line and the full hydro+micro calculation is given by the solid circles, together with PHOBOS data (solid triangles). The shape of the elliptic flow in the pure hydrodynamical calculation at T_{sw} is quite different from that of the full hydrodynamical one terminated at the kinetic freezeout temperature, 110 MeV. Apparently the slight bumps at forward and backward rapidities observed in the full hydrodynamical calculation develop in the later hadronic phase, since it is not observed in the calculation terminated at T_{sw} . Evolving the hadronic phase in the hydro+micro approach increases the elliptic flow at the central rapidities, but not in the projectile and target rapidity regions. As a result, the result for the elliptic flow in the hydro+micro approach is closer to the experimental data, compared to the pure hydrodynamical calculation.

In Fig. 18 we investigate the effect of hadronic rescattering on the duration of the freezeout process by comparing the calculation terminated at T_{sw} without hadronic rescattering (open symbols) and the one including the full hadronic final state in-

interactions (solid symbols). If we terminate time evolution at T_{sw} , most hadrons freezeout around $\tau_f = 10$ fm/c, reflecting the lifetime of the deconfined phase (the tails of the distribution come from the decays of long-lived resonances). The inclusion of hadronic rescattering shifts the peak of the freezeout distribution to larger freezeout times ($\tau_f \sim 20 - 30$ fm), which provides an estimate on the lifetime of the hadronic phase around 10-20 fm.

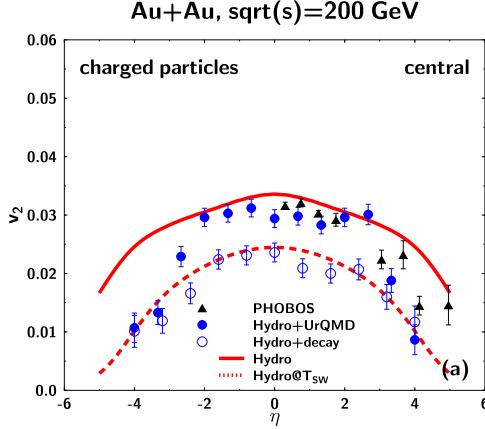


Fig. 17. Elliptic flow as a function of η for π^+ at centralities 5-10 % and 10-20 %. The open symbols stand for STAR data and solid symbols stand for our results.

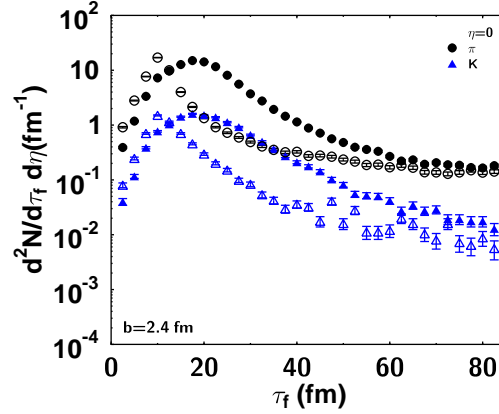


Fig. 18. Freezeout time distribution of mesons for hydro+decay (open symbols) and hydro + UrQMD (solid symbols) at the mid-rapidity in the case of central collisions.

The findings discussed in the context of the previous figure for pions and kaons are confirmed by analyzing baryons in the same way, which is shown in Fig. 19: here the top frame contains the analysis terminated at T_{sw} and the bottom frame contains the calculation including full hadronic rescattering. Figures 18 and 19 suggest that the assumption of sudden freezeout, which is often used, for example, in the blast wave model, is not realistic under the existence of final state interactions.

§7. Summary

In this article, we outlined key issues in constructing a realistic and comprehensive dynamical model for the description of the whole stages of relativistic high energy heavy ion collisions: initial conditions, hydrodynamical expansion, hadronization, and freezeout processes. Hydrodynamical models are a promising starting point for building multi-module models. One of the reasons is that they give global understanding of experimental data at RHIC and their success at RHIC makes us to expect that hydrodynamical analyses will serve as the baseline for investigation also at LHC. In addition, one can easily input up-to-date knowledge on each stage in the time evolution to hydrodynamical models easily: more realistic initial conditions which contain even-by-event fluctuations, latest equations of state and transport coefficients from lattice QCD, realistic hadronization mechanisms such as those from

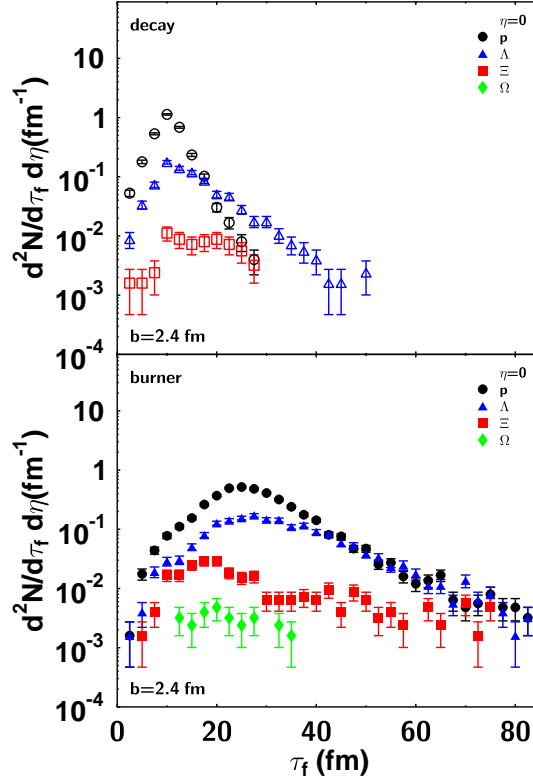


Fig. 19. Freezeout time distribution of baryons for hydro+decay (open symbols, above) and hydro + UrQMD (solid symbols, below) at the mid-rapidity.

the recombination model and fragmentation mechanism, and realistic freezeout processes including final state interactions.

Presently, both ideal and viscous hydrodynamical models are utilized for the investigation of data obtained at RHIC and LHC. In the multi-module modeling, however, ideal hydrodynamical models have been studied more deeply and its status is considered to be more mature than viscous hydrodynamical models. However, gradually the majority of hydrodynamical models will become viscous hydrodynamical models instead of ideal hydrodynamical models, because the study of viscosity effects in physical observables and the estimate of the viscosities in QGP from hadronic observables are among the hottest topics in the field; inclusion of viscosities in hydrodynamics is inevitable for such investigation. At the moment, investigation with viscous hydrodynamical models has just started. Whereas their development is fast and remarkable, a lot of issues remain to be considered, implemented, tested, and improved.

One of them is numerical schemes for solving the relativistic hydrodynamical equation, to which only a little attention has been paid up to now. In particular, the estimate of numerical viscosity is crucial for the study of the viscosities of the matter

created in relativistic heavy ion collisions. In Sec. 4, we showed that SHASTA, KT, and rHLL schemes, which are mainly used in studies of high energy heavy ion collisions, have nearly the same accuracy and numerical artifact. Furthermore, we showed the results of shock tube test with a new numerical scheme which suffers less artificial dissipative effect and showed that it is more suitable for analyses of physical viscosities than SHASTA, KT, and rHLL schemes.

In summary, in this article we discussed essential ingredients in understanding entire stages of high energy heavy ion collisions in detail, together with interpretation of experimental data at SPS, RHIC, and LHC. We hope that the road map shown in this article will serve as a guideline for modeling a realistic dynamical model for high energy heavy ion collisions.

Acknowledgments

We would like to thank Harry Niemi for providing us with their results shown in Figs. 9 and 10. This work was in part supported by Grant-in-Aid for Young Scientists (B) (22740156) and Grant-in-Aid for Scientific Research (S)(2224003) and (C)(23540307).

References

- 1) *First Three Years of Operation of RHIC*, Nucl. Phys. A **757** (2005), 1.
- 2) *Quark Gluon Plasma. New discoveries at RHIC: Case for the Strongly Interacting Quark-Gluon Plasma.*, Nucl. Phys. A **750** (2005), 1.
- 3) Y. Hama, T. Kodama and O. J. Socolowski, Braz. J. Phys. **35** (2005), 24.
- 4) T. Hirano, U. W. Heinz, D. Kharzeev, R. Lacey and Y. Nara, Phys. Lett. B **636** (2006), 299.
- 5) P. Colella and P. R. Woodward, J. Comp. Phys. **54**, 174 (1984).
- 6) L. Baiotti, private communication.
- 7) T. Hirano and Y. Nara, [arXiv:1203.4418v1 [nucl-th]].
- 8) C. Nonaka and S. A. Bass, Phys. Rev. C **75** (2007), 014902.
- 9) T. Hirano, P. Huovinen and Y. Nara, Phys. Rev. C **83**, 021902 (2011) [arXiv:1010.6222 [nucl-th]].
- 10) T. Hirano, P. Huovinen and Y. Nara, Phys. Rev. C **84**, 011901 (2011) [arXiv:1012.3955 [nucl-th]].
- 11) H. Petersen, J. Steinheimer, G. Burau, M. Bleicher and H. Stocker, Phys. Rev. C **78**, 044901 (2008) [arXiv:0806.1695 [nucl-th]].
- 12) H. Holopainen, H. Niemi and K. J. Eskola, Phys. Rev. C **83** (2011), 034901.
- 13) P. Romatschke and U. Romatschke, Phys. Rev. Lett. **99** (2007), 172301.
- 14) K. Dusling and D. Teaney, Phys. Rev. C **77** (2008), 034905.
- 15) M. Luzum and P. Romatschke, Phys. Rev. C **78** (2008), 034915 [Erratum-ibid. Phys. Rev. C **79** (2009), 039903].
- 16) B. Schenke, S. Jeon and C. Gale, Phys. Rev. Lett. **106** (2011), 042301.
- 17) H. Song, S. A. Bass, U. Heinz, T. Hirano and C. Shen, Phys. Rev. Lett. **106** (2011), 192301.
- 18) A. K. Chaudhuri, arXiv:0801.3180v2 [nucl-th].
- 19) V. Roy and A. K. Chaudhuri, Phys. Rev. C **85** (2012), 024909.
- 20) P. Bozek, Phys. Rev. C **85** (2012), 034901.
- 21) R. Baier, A. H. Mueller, D. Schiff and D. T. Son, Phys. Lett. B **502** (2001), 51.
- 22) S. Mrowczynski, **PoS CPOD2006** (2006), 042.
- 23) P. F. Kolb, U. W. Heinz, P. Huovinen, K. J. Eskola and K. Tuominen, Nucl. Phys. A **696** (2001), 197.
- 24) T. Hirano and K. Tsuda, Phys. Rev. C **66** (2002), 054905.

- 25) D. Teaney, J. Lauret and E. V. Shuryak, Phys. Rev. Lett. **86** (2001), 4783.
- 26) J. D. Bjorken, Phys. Rev. D **27** (1983), 140.
- 27) P. F. Kolb and R. Rapp, Phys. Rev. C **67** (2003), 044903.
- 28) U. W. Heinz and P. F. Kolb, preprint arXiv:hep-ph/0204061.
- 29) S. Pratt, Phys. Rev. Lett. **102** (2009), 232301.
- 30) P. F. Kolb, P. Huovinen, U. W. Heinz and H. Heiselberg, Phys. Lett. B **500** (2001), 232.
- 31) P. Huovinen, P. F. Kolb, U. W. Heinz, P. V. Ruuskanen and S. A. Voloshin, Phys. Lett. B **503** (2001), 58.
- 32) T. Hirano and Y. Nara, Nucl. Phys. A **743** (2004), 305.
- 33) L. P. Csernai, Y. Cheng, S. Horvat, V. Magas, D. Strottman and M. Zetenyi, J. Phys. **G36** (2009), 064032.
- 34) K. J. Eskola, H. Honkanen, H. Niemi, P. V. Ruuskanen and S. S. Rasanen, Phys. Rev. C **72** (2005), 044904.
- 35) R. P. G. Andrade, F. Grassi, Y. Hama, T. Kodama and W. L. Qian, Phys. Rev. Lett. **101** (2008), 112301.
- 36) B. I. Abelev *et al.* [STAR Collaboration], Phys. Rev. C **80** (2009), 064912.
- 37) M. P. McCumber and f. t. P. Collaboration, J. Phys. G **35** (2008), 104081.
- 38) J. Takahashi, B. M. Tavares, W. L. Qian, R. Andrade, F. Grassi, Y. Hama, T. Kodama and N. Xu, Phys. Rev. Lett. **103** (2009), 242301.
- 39) S. Mohapatra for the ATLAS Collaboration, [arXiv:1109.6721 [nucl-ex]].
- 40) L. X. Han, G. L. Ma, Y. G. Ma, X. Z. Cai, J. H. Chen, S. Zhang and C. Zhong, Phys. Rev. C **84** (2011), 064907.
- 41) F. G. Gardim, F. Grassi, M. Luzum and J. -Y. Ollitrault, Phys. Rev. C **85** (2012), 024908.
- 42) A. Adare *et al.* [PHENIX Collaboration], Phys. Rev. Lett. **104** (2010), 132301.
- 43) K. Aamodt *et al.* [ALICE Collaboration], Phys. Rev. Lett. **106** (2011), 032301.
- 44) 'Proceedings of Quark Matter 2001', Nucl. Phys. A **698** (2002), 507.
- 45) I. Müller, Z. Phys. **198** (1967), 329.
- 46) W. Israel, Ann. Phys. (N.Y.) **100** (1967), 310.
- 47) W. Israel and J. M. Stewart, Phys. Lett. A **58** (1976), 213.
- 48) W. Israel and J. M. Stewart, Ann. Phys. (N.Y.) **118** (1979), 341.
- 49) M. Grmela and H. C. Öttinger, Phys. Rev. E **56** (1997), 6620.
- 50) H. C. Öttinger and M. Grmela, Phys. Rev. E **56** (1997), 6633.
- 51) H. C. Öttinger, Phys. Rev. E **57** (1998), 1416.
- 52) D. A. Teaney, preprint arXiv:0905.2433 [nucl-th]
- 53) A. Muronga and D. H. Rischke, preprint arXiv:nucl-th/0407114.
- 54) R. Baier, P. Romatschke, D. T. Son, A. O. Starinets and M. A. Stephanov, JHEP **0804** (2008), 100.
- 55) B. Betz, D. Henkel and D. H. Rischke, J. Phys. **G36** (2009), 064029.
- 56) T. Tsumura, T. Kunihiro and K. Ohnishi, Phys. Lett. B **646** (2007), 132.
- 57) K. Tsumura and T. Kunihiro, Phys. Lett. B **668** (2008), 425.
- 58) R. J. Fries, B. Muller and A. Schafer, Phys. Rev. C **78** (2008), 034913.
- 59) H. Song and U. W. Heinz, Phys. Lett. B **693** (2010), 198.
- 60) S. Borsanyi *et al.*, J. High Energy Phys. **1011** (2010), 077.
- 61) A. Bazavov *et al.*, arXiv:1111.1710 [hep-lat].
- 62) T. Umeda *et al.* [WHOT-QCD Collaboration], PoS LATTICE **2010** (2010), 218.
- 63) Z. Fodor and S. Katz, Phys. Lett. B **534** (2002), 87.
- 64) Z. Fodor and S. Katz, J. High Energy Phys. **0203** (2002), 014.
- 65) Z. Fodor, S. Katz, and K. Szabo, Phys. Lett. B **568** (2003), 73.
- 66) Z. Fodor and S. Katz, J. High Energy Phys. **0404** (2004), 050.
- 67) S. Ejiri, Phys. Rev. D **69** (2004), 094506.
- 68) C. Allton, S. Ejiri, S. Hands, O. Kaczmarek, F. Karsch, et. al., Phys. Rev. D **66** (2002), 074507.
- 69) C. Allton, S. Ejiri, S. Hands, O. Kaczmarek, F. Karsch, et. al., Phys. Rev. D **68** (2003), 014507.
- 70) C. Allton, M. Doring, S. Ejiri, S. Hands, O. Kaczmarek, et. al., Phys. Rev. D **71** (2005), 054508.
- 71) R. Gavai and S. Gupta, Phys. Rev. D **71** (2005), 114014.
- 72) WHOT-QCD Collaboration, S. Ejiri et.al., Phys. Rev. D **82** (2010), 014508.

- 73) K. Nagata and A. Nakamura, arXiv:1201.2765 [hep-lat].
- 74) A. Nakamura and S. Sakai, Phys. Rev. Lett. **94** (2005), 072305.
- 75) H. B. Meyer, Phys. Rev. D **76** (2007), 101701.
- 76) P. B. Arnold, G. D. Moore and L. G. Yaffe, J. High Energy Phys. **0011** (2000), 001.
- 77) P. B. Arnold, G. D. Moore and L. G. Yaffe, J. High Energy Phys. **0305** (2003), 051.
- 78) P. B. Arnold, C. Dogan and G. D. Moore, Phys. Rev. D **74** (2006), 085021.
- 79) A. Muronga, Phys. Rev. C **69** (2004), 044901.
- 80) S. Muroya and N. Sasaki, Phys. Rev. D **113** (2005), 457.
- 81) N. Demir and S. A. Bass, Phys. Rev. Lett. **102** (2009), 172302.
- 82) Z. Xu and C. Greiner, Phys. Rev. Lett. **100** (2008), 172301.
- 83) Z. Xu, C. Greiner and H. Stoecker, Phys. Rev. Lett. **101** (2008), 082302.
- 84) K. Itakura, O. Morimatsu and H. Otomo, Phys. Rev. D **77** (2008), 014014.
- 85) R. J. Fries and C. Nonaka, Prog. Part. Nucl. Phys. **66** (2011), 607.
- 86) C. P. Herzog, A. Karch, P. Kovtun, C. Kozcaz and L. G. Yaffe, J. High Energy Phys. **0607** (2006), 013.
- 87) H. Liu, K. Rajagopal and U. A. Wiedemann, Phys. Rev. Lett. **97** (2006), 182301
- 88) S. S. Gubser, Phys. Rev. D **74** (2006), 126005.
- 89) W. A. Horowitz and M. Gyulassy, Phys. Lett. B **666** (2008), 320.
- 90) J. Liao and E. Shuryak, Phys. Rev. Lett. **102** (2009), 202302.
- 91) S. S. Adler et al. (PHENIX Collaboration), Phys. Rev. C **69** (2004), 034909.
- 92) U. Heinz and P. F. Kolb, hep-ph/0204061; P. Huovinen, Nucl. Phys. A **715** (2003), 299c.
- 93) M. Estienne (for the STAR Collaboration), J. Phys. **G31** (2005), S873.
- 94) D. Teaney, nucl-th/0204023.
- 95) K. Adcox et al. (PHENIX collaboration), Nucl. Phys. A **757** (2004), 184.
- 96) S. A. Bass and A. Dumitru, Phys. Rev. C **61** (2000), 064909.
- 97) D. Teaney, J. Lauret, E. V. Shuryak, Phys. Rev. Lett. **86** (2003), 4783; *ibid.*, nucl-th/011037.
- 98) B. B. Back et al. (PHOBOS Collaboration), Phys. Rev. C **72** (2005), 051901(R).
- 99) A. Adare et al. (PHENIX Collaboration), Phys. Rev. Lett. **101** (2008), 232301.
- 100) S. A. Bass, C. Gale, A. Majumder, C. Nonaka, G. Y. Qin, T. Renk and J. Ruppert, Phys. Rev. C **79** (2009), 024901.
- 101) K. Aamodt and C. A. Loizides [ALICE Collaboration], Phys. Lett. B **696** (2011) 30 [arXiv:1012.1004 [nucl-ex]].
- 102) *Riemann Solvers and Numerical Methods for Fluid Dynamics: A Practical Introduction*, Eleuterio, F. Toro, (3rd Ed.), Springer (2009).
- 103) J. P. Boris, D. L. Book, J. Comput. Phys. **11** (1973), 38.
- 104) E. Molnar, H. Niemi and D. H. Rischke, EPJC **65**, 2010, 615.
- 105) Y. Akamatsu, C. Nonaka and M. Takamoto, to be published.
- 106) M. Takamoto and S. Inutsuka, J. Comput. Phys. **230** (2011), 7002.
- 107) *Numerical Hydrodynamics in Special Relativity*, Jose Maria Marti and Ewald Müller, Living Reviews in Relativity, vol. 6, no. 7 (2003).
- 108) J. M. Marti, and E. Müller, Journal of Fluid Mechanics **258** (1994), 317.
- 109) J. Martí, Journal of Computational Physics **123** (1996), 1.
- 110) M. A. Aloy, J. M. Ibañez, J. M. Martí, E. Müller, ApJS **122** (1999), 151.
- 111) J. A. Pons, J. M. Martí, E. Müller, Journal of Fluid Mechanics **422** (2000), 125.
- 112) J. A. Font, M. Miller, W. M. Suen, and M. Tobias, Phys. Rev. D **61** (2000), 044011.
- 113) L. Del Zanna, and N. Bucciantini, Astronomy and Astrophysics **390** (2002), 1177.
- 114) J. M. Martí, E. Müller, Living Reviews in Relativity **6** (2003), 7.
- 115) A. Mignone, and G. Bodo, MNRAS **364** (2005), 126.
- 116) A. Mignone, T. Plewa, and G. Bodo, ApJS **160** (2005), 199.
- 117) T. Inoue, S. Inutsuka, and H. Koyama, ApJ **658** (2007), L99.; T. Inoue, and S. Inutsuka, ApJ **687** (2008), 303; T. Inoue, and S. Inutsuka, ApJ **704** (2009), 161.
- 118) V. Schneider, U. Katscher, D. H. Rischke, B. Waldhauser, J. A. Maruhn and C. D. Munz, J. Comput. Phys. **105** (1993), 92.
- 119) K. S. Lee, S. Bass, B. Muller and C. Nonaka, J. Phys. G **36** (2009), 064034.
- 120) R. J. Fries, M. He and R. Rapp, J. Phys. G **38** (2011), 124068.
- 121) R. C. Hwa and L. Zhu, Phys. Rev. C **84** (2011), 064914.
- 122) R. J. Fries, B. Muller, C. Nonaka and S. A. Bass, Phys. Rev. Lett. **90** (2003), 202303.

- 123) R. J. Fries, B. Muller, C. Nonaka and S. A. Bass, Phys. Rev. C **68** (2003), 044902.
- 124) V. Greco, C. M. Ko and P. Levai, Phys. Rev. Lett. **90** (2003), 202302.
- 125) V. Greco, C. M. Ko and P. Levai, Phys. Rev. C **68** (2003), 034904.
- 126) B. Muller, R. J. Fries and S. A. Bass, Phys. Lett. B **618** (2005), 77.
- 127) L. Ravagli and R. Rapp, Phys. Lett. B **655** (2007), 126.
- 128) R. J. Fries, S. A. Bass and B. Muller, Phys. Rev. Lett. **94** (2005), 122301.
- 129) M. He, R. J. Fries and R. Rapp, arXiv:1006.1111 [nucl-th].
- 130) C. Alt *et al.* [NA49 Collaboration], Phys. Rev. C **75** (2007), 044901.
- 131) M. Krzewicki, J. Phys. G: Nucl. Part. Phys. **38** (2011), 124047.
- 132) C. Nonaka, R. J. Fries and S. A. Bass, Phys. Lett. B **583** (73), 2004.
- 133) S. Shi [STAR Collaboration], Nucl. Phys. A **862-863** (2011), 263C.
- 134) M. Nasim [for the STAR Collaboration], arXiv:1111.7073 [nucl-ex].
- 135) Z. Tang [STAR Collaboration], J. Phys. G **38** (2011), 124107.
- 136) F. Laue [STAR Collaboration], J. Phys. G **31** (2005), S1121.
- 137) C. Nonaka, B. Muller, M. Asakawa, S. A. Bass and R. J. Fries, Phys. Rev. C **69** (2004), 031902.
- 138) J. Adams *et al.* [STAR Collaboration], Phys. Rev. C **71** (2005), 064902 .
- 139) C. Nonaka, B. Muller, S. A. Bass and M. Asakawa, Phys. Rev. C **71** (2005), 051901.
- 140) M. Asakawa and T. Hatsuda, Phys. Rev. Lett. **92** (2004), 012001.
- 141) S. Datta, F. Karsch, P. Petreczky and I. Wetzorke, Phys. Rev. D **69** (2004), 094507.
- 142) H. Iida, T. Doi, N. Ishii, H. Suganuma and K. Tsumura, Phys. Rev. D **74** (2006), 074502.
- 143) T. Umeda, Phys. Rev. D **75** (2007), 094502.
- 144) J. Adams *et al.* (STAR Collaboration), Phys. Rev. C **68** (2003), 044905; G. D. Westfall (STAR Collaboration), J. Phys. G **30**(2004)S1389.
- 145) K. Adcox *et al.* (PHENIX Collaboration), Phys. Rev. Lett. **89** (2002), 082301; J. Nystrand (PHENIX Collaboration), Nucl. Phys. A **715** (2003), 603.
- 146) See e.g. P. Braun-Munzinger, K. Redlich, J. Stachel, in *Quark Gluon Plasma 3*, (Eds. R. C. Hwa and X. N. Wang, World Scientific)
- 147) A. Andronic, P. Braun-Munzinger, K. Redlich and J. Stachel, J. Phys. G **38** (2011), 124081.
- 148) F. Becattini, arXiv:0901.3643 [hep-ph].
- 149) F. Cooper, G. Frye, Phys. Rev. D **10** (1974), 186.
- 150) O. J. Socolowski, F. Grassi, Y. Hama and T. Kodama, Phys. Rev. Lett. **93** (2004), 182301.
- 151) J. Adams *et al.* [STAR Collaboration], Phys. Rev. Lett. **92** (2004), 112301.
- 152) U. W. Heinz and P. F. Kolb, Nucl. Phys. A **702** (2002), 269.
- 153) N. Arbex, F. Grassi, Y. Hama, O. Socolowski, preprint arXiv:nucl-th/0102056
- 154) N. Arbex, F. Grassi, Y. Hama and O. Socolowski, Phys. Rev. C **64** (2001), 064906.
- 155) S. A. Bass and A. Dumitru, Phys. Rev. C **61** (2000), 064909.
- 156) D. Teaney, J. Lauret and E. V. Shuryak, arXiv:nucl-th/0110037.
- 157) M. Estienne (for the STAR Collaboration), J. Phys. **G31** (2005), S873.
- 158) J. Adames *et al.* (STAR Collaboration), Phys. Rev. Lett. **92** (2004), 182301.
- 159) H. van Hecke, H. Sorge and N. Xu, Phys. Rev. Lett. **81** (1998), 5764.
- 160) A. Dumitru, S. A. Bass, M. Bleicher, H. Stoecker and W. Greiner, Phys. Lett. B **460** (1999), 411.
- 161) P.G. Jones and the NA49 collaboration, Nucl. Phys. A **610** (1996), 188c;
C. Bormann *et al.*, (NA49 collaboration), J. Phys. **G23**(1997)1817;
H. Appelshäuser *et al.*, (NA49 collaboration), Phys. Lett. B **444** (1998), 523;
E. Andersen *et al.* (WA97 Collaboration), Phys. Lett. B **433** (1998), 209;
E. Andersen *et al.* (WA97 Collaboration), J. Phys. **G25**(1999)181.